Atmos. Meas. Tech. Discuss., doi:10.5194/amt-2015-387, 2016
Manuscript under review for journal Atmos. Meas. Tech.
Published: 18 January 2016

Atmospheric Measurement Techniques
Discussions

New methods for retrieval of chlorophyll red fluorescence from hyper-spectral satellite instruments: simulations and application to GOME-2 and SCIAMACHY

J. Joiner[1], Y. Yoshida[2], L. Guanter[3], and E. M. Middleton[1]

[1]NASA Goddard Space Flight Center, Greenbelt, MD, USA
[2]Science Systems and Applications, Inc., Lanham, MD, USA
[3]Helmholtz Centre, Potsdam, Germany

Correspondence to: J. Joiner (joanna.joiner@nasa.gov)

Abstract.

Global satellite measurements of solar-induced fluorescence (SIF) from chlorophyll over land and ocean have proven useful for a number of different applications related to physiology, phenology, and productivity of plants and phytoplankton. Terrestrial chlorophyll fluorescence is emitted throughout the red and far-red spectrum, producing two broad peaks near 683 and 736 nm. From ocean surfaces, phytoplankton fluorescence emissions are entirely from the red region. Studies using satellite-derived SIF over land have focused almost exclusively on measurements in the far- red, since those are the most easily obtained with existing instrumentation. Here, we examine new ways to use existing hyper-spectral satellite data sets to retrieve red SIF over both land and ocean. Our approach offers noise reductions as compared with previously published solar line filling retrievals by making use of the oxygen (O_2) γ-band that is not affected by SIF. The O_2 γ-band in conjunction with solar Fraunhofer lines help to anchor the O_2 B-band that provides additional information on red SIF. Biases due to instrumental artifacts that vary in time, space, and with instrument, must be addressed in order to obtain reasonable results. The satellite instruments that we use were designed to make atmospheric trace- gas measurements and are therefore not optimal for observing SIF; they have coarse spatial resolution and only moderate spectral resolution ($\sim$0.5 nm). Nevertheless, these instruments offer a unique opportunity to compare red and far-red terrestrial SIF at regional spatial scales. Our eight year record of red SIF observations over land with the Global Ozone Monitoring Instrument 2 (GOME-2) allows for the first time reliable global mapping of monthly anomalies. These anomalies are shown to have similar spatio-temporal structure as those in the far-red, particularly for drought-prone regions. There is a somewhat larger percentage response in the red as compared with the far-red for these areas that are sensitive to soil moisture, although the differences are within the specified uncertainties that are dominated by systematic errors. We also demonstrate that high quality ocean fluorescence line height retrievals can be achieved with GOME-2 and similar instruments by utilizing the full complement of radiance measurements that span the red SIF emission feature.

Atmos. Meas. Tech. Discuss., doi:10.5194/amt-2015-387, 2016
Manuscript under review for journal Atmos. Meas. Tech.
Published: 18 January 2016

Atmospheric Measurement Techniques Discussions

1 Introduction

Measurements of chlorophyll fluorescence over both land and ocean are related to photosynthetic function and thus the carbon cycle and climate feedbacks. Observations of solar induced fluorescence (SIF) from chlorophyll, obtained from specialized satellites, can provide global coverage within a few days at spatial scales relevant to global models ($\sim 0.5° \times 0.5°$ grid cells). Satellite instruments that have been utilized to measure chlorophyll SIF over land include the the MEdium Resolution Imaging Spectrometer (MERIS) (Guanter et al., 2007), the Japanese Greenhouse gases Observing SATellite (GOSAT) (Joiner et al., 2011, 2012; Frankenberg et al., 2011b; Guanter et al., 2012), the SCanning Imaging Absorption spectroMeter for Atmospheric CHartographY (SCIAMACHY) (Joiner et al., 2012; Köhler et al., 2015; Wolanin et al., 2015), the Global Ozone Monitoring Experiment-2 (GOME-2) (Joiner et al., 2013), and the Orbiting Carbon Observatory 2 (OCO-2) (Frankenberg et al., 2014). Terrestrial SIF derived from these satellites has been used for studies focused on tropical dynamics (Parazoo et al., 2013; Guan et al., 2015a), primary productivity (Guanter et al., 2014; Parazoo et al., 2014; Zhang et al., 2014; Lee et al., 2015; Guan et al., 2015b), the carbon uptake period (Joiner et al., 2014), and responses to drought (Lee et al., 2013; Yoshida et al., 2015; Sun et al., 2015). Oceanic SIF measurements have been made with MERIS (Gower and King, 2007), SCIAMACHY, GOME-2 (Wolanin et al., 2015), the MODerate-resolution Imaging Spectroradiometer (MODIS) (Abbott and Letelier, 1999), and the Korean Geostationary Ocean Color Imager (GOCI) (O'Malley et al., 2014). MODIS has been used to detect red tides (e.g., Hu et al., 2005) and to conduct studies related to the physiology, phenology, and productivity of phytoplankton (e.g., Behrenfeld et al., 2009; Morrison and Goodwin, 2010; Gower and King, 2012; McKibben et al., 2012; Westberry et al., 2013; O'Malley et al., 2014; Gower, 2015).

In terrestrial vegetation, chlorophyll fluorescence is emitted at red to far-red wavelengths with two broad peaks near 685 and 740 nm, known as the red and far-red emission features, respectively, as shown in Fig. 1. Oceanic SIF is emitted in the red emission feature. The primary method used to measure the small terrestrial fluorescence signal from passive ground- and aircraft- remote sensing instrumentation makes use of dark features in spectra of reflected sunlight from oxygen absorption bands in the Earth's atmosphere (see e.g. Meroni et al., 2009, and references therein). The strong O_2 A-band (~ 760 nm) and its somewhat weaker counterpart, the O_2 B-band (~ 690 nm), are conveniently located near the peaks of the far-red (but displaced $\sim$20 nm) and red (< 5 nm) chlorophyll fluorescence emission features, respectively (see Fig. 1).

Solar Fraunhofer lines, also shown in Fig. 1, have also been used to measure SIF from the ground (e.g., Guanter et al., 2013) and from space (Joiner et al., 2011, 2012; Frankenberg et al., 2011b, 2014; Guanter et al., 2012; Joiner et al., 2013). Use of the filling-in of solar Fraunhofer lines for satellite retrievals has several advantages as compared with that from oxygen absorption features. Firstly, the spectral structure of solar lines is not modified by clouds, aerosols, surface pressure, or temperature as is the case with atmospheric oxygen absorption features (e.g., Preusker and Lindstrot, 2009; Joiner et al., 2011; Frankenberg et al., 2011a). Secondly, SIF emissions are partially absorbed in the atmosphere as they travel towards a satellite sensor at wavelengths where oxygen (and water vapor) are radiatively active. Satellite SIF retrieval algorithms that rely mostly or exclusively on solar lines tend to be less complex than those that rely primarily on measurement of the signal in the O_2 A- and B-bands. To effectively utilize these O_2 bands, both the downward and upward transmittance through the atmosphere must be accurately

Atmos. Meas. Tech. Discuss., doi:10.5194/amt-2015-387, 2016
Manuscript under review for journal Atmos. Meas. Tech.
Published: 18 January 2016

estimated. Satellite SIF studies to date that rely primarily on these bands have either required an on-ground non-fluorescing target (Guanter et al., 2007) or have used only simulated conditions to retrieve some or all of the parameters affecting the bands (Guanter et al., 2010; Sanders and de Haan, 2013; ESA, 2015; Cogliati et al., 2015).

Nearly all scientific studies utilizing space-based terrestrial SIF have thus far focused entirely on retrievals from the far-red fluorescence feature. While far-red SIF has been shown to be useful for several applications, having the combination of both red and far-red SIF observations may offer additional information. For example, the relative magnitudes of the red and far-red peaks and their emission intensities are sensitive to nitrogen uptake (Corp et al., 2003, 2006, 2010; Campbell et al., 2007, 2008; Zarco-Tejada et al., 2003) and responses to stresses including low temperature and high salinity (Agati et al., 1995, 1996, 2000; Lichtenthaler, 1987, 1988, 1996; Rinderle and Lichtenthaler, 1988). Ač et al. (2015) conducted meta-analysis of stress responses to red and far-red passively and actively sensed fluorescence signals for both leaf and canopy measurements. Their results indicate, for example, a higher detectability of water stress in the far-red as compared with the red fluorescence, consistent with observations of Daumard et al. (2010), Fournier et al. (2012), Middleton et al. (2015) and references within that showed influences of canopy architecture on far-red fluorescence signals. As noted, red and far-red canopy fluorescence measurements may reflect information from different layers of a canopy or leaf (Gitelson et al., 1998; Porcar-Castell et al., 2014) owing to higher amounts of reabsorption at red wavelengths. This may lead to higher sensitivity of the far-red signal to deeper layers of the canopy (Verrelst et al., 2015). While most fluorescence is emitted from photosystem II (PS II), a protein complex involved in photosynthesis, Agati et al. (2000) discuss the impact of photosystem I (PSI) and temperature sensitivity on the ratio of far-red to red fluorescence emissions. The PSI contribution grows with wavelength and is considered to be unaffected by biochemstry while the PSII contribution is affected by both physiological regulation as well as leaf structure and chemical composition (Verrelst et al., 2015). In a canopy radiative tranport model, Verrelst et al. (2015) then show that the carboxylation capacity (V_{cmo}), related to photosynthetic capacity, has its greatest influence in the red emission peak. They further suggest that when trying to relate SIF to photosynthetic quantaties such as gross primary productivity (GPP), it would be more beneficial to exploit the full broadband emission flux as compared with a single band in the far-red.

SIF emissions must be understood and accounted for in order to make the best possible use oxygen bands for atmospheric applications. For example, the O_2 A-band has been used to estimate aerosol plume height (e.g., Sanders et al., 2015). The O_2 A-band has also been used to assess photon pathlength for trace-gas retrievals including CO_2 (e.g., O'Dell et al., 2012). It is for this purpose that the A-band spectral region is specifically observed with several atmospheric satellite sensors. Unfortunately for SIF retrieval, some of these instruments, such as GOSAT and OCO-2, include only the O_2 A-band and not the B-band. However, GOME-2 and SCIAMACHY include both bands.

Terrestrial SIF retrievals near the red peak can have larger errors than those near the far-red peak for several reasons. Firstly, solar Fraunhofer features are not as wide and deep in the red region as those in the far-red; this makes the red solar Fraunhofer features less sensitive to filling-in by SIF, particularly at the moderate spectral resolution (full width at half maximum, FWHM, of ∼0.5 nm) of current satellite sensors such as GOME-2 and SCIAMACHY that have spectral coverage in the red region. Secondly, the O_2 B-band covers a fairly large section of the SIF near the peak within the red fluorescence emission feature. Therefore, less spectral range near the red peak is available for the straightforward solar Fraunhofer line retrieval approach as compared with the far-red. Thirdly, the sharp upturn of the red-edge in reflectance (see Fig. 1) may complicate retrievals. For example, it may necessitate the use of smaller rather than larger spectral fitting windows for Fraunhofer line retrievals. Finally, at lower reflectances of the red band as compared with the far-red, effects of dark current and stray light may constitute a larger percentage of the overall observed radiance leading to larger systematic errors.

Results of simulated red SIF retrievals performed for the TROPOspheric Monitoring Instrument (TROPOMI), a hyper-spectral grating instrument to be launched in 2016, show that it should have capability to retrieve red SIF using relatively small spectral fitting windows (Guanter et al., 2015). Wolanin et al. (2015) showed that a red SIF signal can be detected from SCIAMACHY and GOME-2 using a spectral fitting window of 681.8–685.5 that is located close to the red SIF emission peak but just outside the O_2 B-band. Results for a single month show spatial patterns similar to those of the Enhanced Vegetation Index (EVI). While promising, the monthly averages appear to be noisy, and a significant offset between GOME-2 and SCIAMACHY red SIF magnitudes was shown (Wolanin et al., 2015). Some of these difficulties in retrieving red SIF should be overcome with the higher spectral resolution instruments designed specifically for fluorescence retrievals ($\leq$ 0.3 nm) planned with the Fluorescence Explorer (FLEX) mission, as recently shown with modeling studies (Cogliati et al., 2015).

Here, we develop new methodology to retrieve terrestrial red SIF using space-based hyper-spectral measurements, especially useful for implementation with moderate spectral resolution data currently available. The approaches make use of solar Fraunhofer line filling and absorption in and around the O_2 B- (or A-) bands. Absorption of sunlight in atmospheric absorption bands is complicated due to photon path modulation by aerosol and cloud profiles, surface pressure, and surface effects such as the bi-directional reflectance distribution function (BRDF). Our new methodology additionally makes use of the relatively weak O_2 γ-band spectral region, near 627 nm, essentially as an additional anchor to estimate the amount of absorption that will be present in the O_2 B- (or A-) bands. The O_2 γ-band occurs in a spectral valley between red and blue-green fluorescence features (e.g., Lichtenthaler and Schweiger, 1998) and so has a minimal sensitivity to vegetation fluorescence. This band also has a minor sensitivity to water vapor absorption as is the case for the O_2 B-band (see Fig. 1).

Our methodology is similar to approaches developed for ground- and satellite-based instruments in that radiative transfer in atmospheric absorption bands is approximated using a data-driven principal component analysis (PCA) approach (Guanter et al., 2012; Joiner et al., 2013; Köhler et al., 2015). Similar PCA methods have also been applied to retrievals of atmospheric trace gases (Li et al., 2013, 2015). While our approach does not require a nearby non-fluorescing target, it does make use of a representative sample of observations over non-fluorescing scenes in order to generate a comprehensive set of fluorescence-free principal components (PCs). For this purpose, we use desert and snow- or ice-covered data over land as well as cloudy observations over ocean covering a large range of latitudes and conditions. While our approach is generally applicable to either the O_2 A- or B-band spectral regions, we focus here on the B-band. The O_2 A-band has more non-linear absorption (saturated lines) and tends to be brighter than the O_2 B- or γ-bands over vegetated land (see Fig. 1); this may lead to complex photon path differences for the O_2 A-band as compared with the B-band in the presence of cloud and aerosol. In addition, SIF can be accurately retrieved with existing satellite instrumentation in the far-red emission feature without need of the O_2 A-band by utilizing the filling-in of solar Fraunhofer lines (Joiner et al., 2013). In contrast, current moderate spectral resolution satellite

Atmos. Meas. Tech. Discuss., doi:10.5194/amt-2015-387, 2016
Manuscript under review for journal Atmos. Meas. Tech.
Published: 18 January 2016

retrievals using Fraunhofer features near the red emission peak suffer from high noise and systematic errors (Wolanin et al., 2015). Our methods offer a potentially more sensitive approach.

We conduct simulations to demonstrate the applicability of our approach to current and future satellite instruments. We then apply our technique to data from SCIAMACHY on the European Space Agency (ESA) Environmental Satellite (Envisat) and GOME-2 on the European Meteorological Satellite (EuMetSat) first operational MetOp-A satellite. The primary function of these instruments was and is to make measurements of atmospheric trace gases. While not optimal for fluorescence retrievals owing to their relatively large ground footprints and moderate spectral resolution, their excellent ground sampling, large spectral coverages, and high signal-to-noise ratios enable red SIF retrievals. Near-global coverage is provided within a few days from GOME-2 and SCIAMACHY measurements. Application of our approach leads to unprecedented precision and accuracy for red SIF data sets that span more than a decade. We also show that these sensors can be used to make high quality measurements of fluorescence line height over the ocean by utilizing their full spectral content covering the range of red SIF emissions.

2 GOME-2 and SCIAMACHY satellite data

We use data from GOME-2, a nadir-viewing cross-track scanning spectrometer that measures radiances at wavelengths from the ultraviolet to the near-infrared (240–790 nm) (Munro et al., 2006). It flies on the series of European Meteorological Satellites (EUMETSAT) as part of the Polar System (EPS) MetOp mission. GOME-2 measures the solar irradiance and backscattered radiance from the Earth in four detector channels. Here, we use revision R2 level 1B data from channel 4 that covers wavelengths 590–790 nm with a spectral resolution of approximately 0.5 nm (Callies et al., 2000). The signal-to-noise ratio (SNR) in this channel is fairly high (> 1000). The footprint size on the Earth's surface at nadir view is approximately $40\,\mathrm{km} \times 80\,\mathrm{km}$ in its nominal mode with a swath width of 1920 km. In this mode, it takes about 1.5 days for a single GOME-2 instrument to provide coverage of Earth's surface globally.

The first GOME-2 instrument was launched on the MetOp-A satellite 19 October 2006. MetOp satellites are in a polar orbit with an equator crossing local time near 09:30 LT. The second GOME-2 was launched 17 September 2012 on the MetOp-B platform that has a similar equator crossing time but is 180° out of phase with respect to the first flight model. Therefore, one or the other of the GOME-2 instruments is making observations of the sunlit part of the Earth. Near daily global coverage is provided by the two instruments. Since 15 July 2013, GOME-2 onboard MetOp B makes observations in the nominal mode, while the MetOp A GOME-2 measures in a reduced swath of 960 km with a nadir pixel size of $\sim$40 km by 40 km.

SCIAMACHY is a similar grating spectrometer that makes measurements in both limb- and nadir-viewing geometries from ultraviolet to near-infrared wavelengths (212–2386 nm) in eight separate channels (Lichtenberg, 2006). It was launched in February 2002 on Envisat and took measurements until 8 April 2012 when communication with the host satellite was suddenly lost. Envisat flew in a sun-synchronous orbit with a descending node equator crossing time near 10:00 LT. In this work, we use channel 4 that covers wavelengths between 595 and 812 nm at a spectral resolution of 0.48 nm. The nadir ground footprint size is approximately 30 km by 60 km in the along and across track directions, respectively, for latitudes between 60 N and 60

Atmos. Meas. Tech. Discuss., doi:10.5194/amt-2015-387, 2016
Manuscript under review for journal Atmos. Meas. Tech.
Published: 18 January 2016

Atmospheric Measurement Techniques Discussions

S. We use the SciaL1c command-line tool software package (DLR, 2006) to apply all available corrections and calibrations to generate level 1B data.

3 Simulated radiances and irradiances

To test the algorithm and accurately quantify retrieval errors, we use radiance simulations over a wide range of conditions as in Joiner et al. (2013) and Guanter et al. (2015) but now including wavelengths in and surrounding the O_2 γ band. Here, we provide a brief overview of the simulated data. Top-of-the-atmosphere (TOA) radiances are computed using the Matrix Operator Model (MOMO) radiative transfer model (Fell and Fischer, 2001; Preusker and Lindstrot, 2009) with absorption line parameters from the high-resolution atmospheric radiance and transmittance model code (HITRAN) 2008 dataset (Rothman et al., 2009). The monochromatic sun-normalized radiances are sampled at 0.005 nm. They are then multiplied by a solar spectrum sampled in the same way and finally convolved with various instrument line shape functions and resampled. Neither rotational-Raman scattering (RRS) nor O_2 A-band dayglow emissions are included as they are relatively small at the wavelengths of interest (Vasilkov et al., 2013; Guanter et al., 2010). Directional effects of the vegetation reflectance and fluorescence are also not simulated.

Radiances are computed for a range of view and solar zenith angles, atmospheric temperatures, humidities, aerosol profiles, and surface pressures as discussed in Joiner et al. (2013). Two separate data sets are created, one without fluorescence intended for principal component analyses (referred to as “training”), and one containing fluorescence intended to examine retrieval performance (referred to as “testing”). There are sixty top-of-canopy fluorescence spectra from various combinations of chlorophyll content and leaf area index (LAI) as shown in Joiner et al. (2013). There are a total of 38 400 and 230 400 different samples in the training and testing data sets, respectively.

4 Retrieval methodology

We performed several types of red SIF retrievals using both real satellite data and simulations. The first type, referred to as O_2 red SIF retrievals, uses spectral fitting windows encompassing O_2 γ- and B-bands. The fitting windows are 622-640 nm for the O_2 γ and between 682 and 698 nm for the O_2 B-band. This approach is applicable to terrestrial SIF retrievals. The second type of red SIF retrieval is similar to that used by Joiner et al. (2013) for far-red SIF retrievals and Guanter et al. (2015) for simulated TROPOMI red SIF retrievals employing a relatively small fitting window (682-686.5 nm). This window is similar to the one used by Wolanin et al. (2015) in a differential optical absorption spectroscopy (DOAS) type of retrieval applied to GOME-2 and SCIAMACHY. We refer to this approach as the solar line red SIF retrieval.

Our approach for ocean retrievals uses the full spectral window of 660–713 nm and does not require the use of the O_2 γ-band spectral window. Instead, this approach for ocean retrievals primary exploits the continuum SIF emission that includes both sides of the 683 nm feature. This emission can be cleanly detected over the relatively dark ocean surface.

Atmos. Meas. Tech. Discuss., doi:10.5194/amt-2015-387, 2016
Manuscript under review for journal Atmos. Meas. Tech.
Published: 18 January 2016

Atmospheric Measurement Techniques Discussions

4.1 General approach

The basic idea behind our approach is similar that used by Joiner et al. (2013). The key is to separate the spectral features of sun-normalized top-of-atmosphere (TOA) radiances ($\rho_{\rm tot}$) as a function of wavelength λ related to 1) atmospheric absorption (i.e., the total irradiance transmittance $\mathcal{T}$ and the spherical transmittance from surface to TOA, $\overline{\mathcal{T}}$; 2) surface reflectivity ($\rho_{\rm s}$); and 3) SIF radiance emitted at the surface. Neglecting the effects of atmospheric scattering, which was shown to be appropriate in this context (Joiner et al., 2013), we have

$$\rho_{\rm tot}(\lambda) = \rho_{\rm s}(\lambda)\mathcal{T}(\lambda)\overline{\mathcal{T}}(\lambda) + \frac{\pi \mathrm{SIF}(\lambda)\overline{\mathcal{T}}(\lambda)}{E(\lambda)\cos(\theta_0)}, \tag{1}$$

where θ_0 is the solar zenith angle (SZA), and $E(\lambda)$ is the observed extraterrestrial solar irradiance. Joiner et al. (2013) showed that $\overline{\mathcal{T}}(\lambda)$ could be estimated using

$$\overline{\mathcal{T}}(\lambda) = \exp\left(\ln\left[\mathcal{T}_2(\lambda)\right]\frac{\sec(\theta)}{\sec(\theta)+\sec(\theta_0)}\right), \tag{2}$$

where θ is the view zenith angle, and $\mathcal{T}_2(\lambda) = \mathcal{T}(\lambda)\overline{\mathcal{T}}(\lambda)$ is the sun to satellite (2-way) atmospheric transmittance. This amounts to the assumption of the so-called geometrical air mass factor within the DOAS formulation that is appropriate for a non-scattering, linearly absorbing atmosphere. With atmospheric scattering, $\rho_{\rm s}(\lambda)$ and $\mathrm{SIF}(\lambda)$ represent TOA spectral components of surface reflectance and fluorescence modified by atmospheric scattering that is spectrally smooth.

Here, we model the fluorescence red emission feature as having a Gaussian shape similar to e.g., Subhash and Mohanan (1997) and Zarco-Tejada et al. (2000), i.e.,

$$\mathrm{SIF}(\lambda) = \exp\left(\frac{(\lambda-\lambda_0)^2}{2\sigma^2}\right). \tag{3}$$

For the red fluorescence emission feature, we use $\lambda_0 = 683$ nm. Over ocean, we found that a value for the Gaussian standard deviation, σ, of 9.55 nm provided a good fit to observations. Over land, we found that interference from the far-red SIF emission feature may necessitate the use of different values of σ depending on the size of the spectral fitting window as discussed below.

As in Joiner et al. (2013), we assume that $\rho_{\rm s}(\lambda)$, within our limited spectral fitting window, is spectrally smooth and model it as a low order polynomial in λ. While other representations for fluorescence and reflectance have been explored (e.g., Mazzoni et al., 2010, 2012), small errors in the assumed shape of the fluorescence emission will likely have little impact on the estimated peak fluorescence value (Daumard et al., 2010; Fournier et al., 2012; Guanter et al., 2013). We estimate the spectral structure of $\mathcal{T}_2$ using principal components (PCs) as described below.

4.2 Generation of atmospheric PCs

Here, we use a data-driven approach to estimate $\mathcal{T}_2(\lambda)$ in Eq. 2. We perform a principal component analysis (PCA) to represent $\mathcal{T}_2(\lambda)$ similar to the approach of Joiner et al. (2013) and Köhler et al. (2015), i.e.,

$$\mathcal{T}_2(\lambda) = \sum_{i=1}^{n} a_i\phi_i(\lambda) + 1, \tag{4}$$

where $\phi_i(\lambda)$ are the principal components (PCs) and a_i are the coefficients of the PCs. In place of laboratory-measured absorption cross-sections as is typical in the DOAS approach, we are essentially using atmospheric spectra (simulated or measured) to derive the spectral components of atmospheric absorption. This approach has the following advantages: 1) it does not require knowledge of the instrument response function and 2) it implicitly captures instrumental artifacts such as drifts and imperfections in the wavelength calibration.

For comparison, we performed the PCA with both the simulation training data and actual GOME-2 radiances. For the GOME-2 PCA, we use spectra from a single day consisting of observations over sea ice, snow/ice-covered land, the Sahara desert, and cloudy ocean for pixels with $\theta_o < 75°$. For the cloudy ocean data, we compute the reflectance at 670 nm (ρ_{670}) and use observations only for $\rho_{670} > 0.7$.

Joiner et al. (2013) used the logarithm of the normalized radiance spectra as is typical in DOAS implementations. Here, we work with the normalized radiances rather than the logarithm of the normalized radiance as this works just as well. For both real and simulated data, we normalize the spectra with respect to second order polynomials fit to wavelengths not significantly affected by atmospheric absorption (i.e., $620 < \lambda < 625$ nm, $635 < \lambda < 640$ nm, 680$< \lambda < 687$ nm, $712 < \lambda < 713$ nm). This essentially produces atmospheric transmittance spectra. We then subtract unity before conducting the principle component analysis to produce values of zero in the absence of atmospheric absorption. The value of unity is then added back in the retrieval step once the coefficients of the PCs are determined in order to compute the two-way transmittance. In the strict implementation of PCA, a mean spectrum is computed and subtracted from each spectrum. We found that this is not necessary and in fact further complicates the approach. When the mean is not subtracted, the first PC represents the mean atmospheric transmittance.

One key difference with respect to the approach used by Joiner et al. (2013) is that here we use two separate and disconnected spectral regions, encompassing the O_2 γ- and B-bands, to retrieve SIF in the red emission feature over land. For these two fitting windows, a single PCA in performed that covers both fitting windows. The purpose of the PCA is to relate the absorption in the O_2 γ- and B-bands in the absence of fluorescent emissions. Then, in the retrieval step the O_2 γ-band can be used as an anchor to estimate the spectral structure of the O_2 B-band. This is done simultaneously with the retrieval of red SIF and the surface spectral reflectance. Equation 2 is used to estimate how much of the SIF emission is absorbed within the atmosphere as it travels towards the satellite sensor.

Figure 2 shows the leading four PCs for the wavelength ranges 622-640 nm and 680-713 nm that encompass the O_2 γ- and B-bands, respectively. The PCs are computed with simulated data for FWHMs of 0.5 nm (similar to GOME-2) and 0.3 nm and well as with actual GOME-2 data from 1 July 2012. The spectral variance in these window is due to both oxygen and water vapor absorption. The variances explained (with respect to the total) as well as the cumulative variances explained are indicated. The PCs for the simulated data are similar for the two spectral resolutions with more fine-scale structure, particularly in the oxygen B-band, at the higher resolution. The variance explained by the leading PCs is similar for the simulated data at the two spectral resolutions and for GOME-2 data, with slightly more variance explained per PC for GOME-2 data. The first PC explains over 96 % of the spectral variance. More than 99.97 % of the variance is captured in the first four modes for both the simulated and GOME-2 data.

Atmos. Meas. Tech. Discuss., doi:10.5194/amt-2015-387, 2016
Manuscript under review for journal Atmos. Meas. Tech.
Published: 18 January 2016

Atmospheric Measurement Techniques Discussions

The PCs for simulated and real data are not expected to be identical. PCs from the real data may contain instrumental artifacts and processes not included in the simulated data (e.g., rotational-Raman scattering). In addition, the simulated data may not represent all of the conditions or the distribution of conditions that are present in the GOME-2 data. It is never-the-less remarkable how similar the leading PCs are in the simulated data as compared with the GOME-2 data.

4.3 Solving the non-linear problem

As described in Joiner et al. (2013), we use a gradient-expansion algorithm to solve the non-linear estimation problem using a forward model based on Eqs. 1-**??**. The observation vector for each pixel consists of sun-normalized radiances in two separate windows, encompassing the O_2 γ and B-bands. In general, the state vector consists of 1) coefficients of the PCs, 2) separate sets of coefficients for surface reflectance polynomials in the two windows, and 3) the peak value of the red fluorescence feature centered at ~683 nm. At convergence, the partial derivatives contained in the Jacobian $\mathbf{K}$ matrix may be used to compute errors from an unconstrained linear error estimation, i.e.,

$$\mathbf{S}_{\mathrm{r}} = \left(\mathbf{K}^T \mathbf{S}_{\mathrm{e}}^{-1} \mathbf{K}\right)^{-1}, \tag{5}$$

where $\mathbf{S}_{\mathrm{r}}$ is the retrieval error covariance matrix, and $\mathbf{S}_{\mathrm{e}}$ is the measurement error covariance.

Specifically, the state vector of the solar line red SIF terrestrial retrievals consist of coefficients for a third order polynomial to model the surface reflectivity, coefficients for 3 PCs, and a mean value of SIF across the small fitting window (i.e., the Gaussian shape for SIF emission is not needed or used). In contrast, the state vector for the more complex O_2 terrestrial red SIF satellite retrievals includes coefficients of 15 PCs, coefficients of a fourth order polynomial for surface reflectivity in each O_2 fitting region, and the peak value of SIF at 683 nm assuming a Gaussian shape for SIF emissions at red wavelengths. The fitting windows used for GOME-2 and SCIAMACHY were 622–640 nm for the O_2 γ band region and 682–692 nm for the B-band region. We used $\lambda_0 = 683$ nm and $\sigma = 10$ for the satellite retrievals. The selection of these parameters will be discussed in more detail below.

For oceanic retrievals, coefficients of 8 PCs are retrieved along with those of a second order polynomial to account for the spectral dependence of the water leaving radiance. The fitting window 660–713 nm spans the range of significant red SIF emissions. We use Eq. 3 with $\lambda_0 = 683$ nm and $\sigma = 9.55$ for oceanic SIF emissions. We found that these parameter values provide good fits to the observed radiances over ocean.

4.4 Processing of GOME-2 and SCIAMACHY data

The overall processing of the satellite data follows the approach detailed in Joiner et al. (2013) which is augmented as described in this section. Figure 3 show a flow diagram of the basic steps. One subset of radiance data is used to generate the PCs (chosen such that fluorescence is not present). We perform a PCA daily using its corresponding daily-measured solar irradiance. Similar to Joiner et al. (2013), we use pixels over highly cloudy ocean and snow- and ice-covered surfaces (ρ at 670 nm > 0.7 and SZA $< 70°$) and the Sahara for the PCA. The derived PCs are then used for the fluorescence retrieval. Quality assurance checks and bias adjustments are then conducted to filter out cloudy data and failed retrievals and remove biases as described in Joiner et al.

(2013) and below in Sect. 4.4.2. Finally, the quality controlled retrievals are gridded at a monthly temporal and 1°(or other as noted) spatial resolution to produce level 3 data sets.

Ideally, the last step is validation of the level 2 or 3 data sets. There are very few opportunities for validation available. Yang et al. (2015) compared ground-based data with far-red SIF from GOME-2 for a season over one forested location. But in general, it is difficult to compare ground-based data with large pixel satellite data owing to the spatial mismatch. Aircraft-based data are extremely limited at the current time. One of the few tools available for global validation is intercomparison of different satellite data sets as in Joiner et al. (2013) and Köhler et al. (2015) which is the approach undertaken here.

4.4.1 Absolute solar calibration drift

Many instrumental calibration issues cancel out when using the ratio of the Earth radiance to the solar irradiance (i.e., reflectances) in Eq. 1. For example, the reflectance degradation factor at the wavelengths of interest for GOME-2 SIF retrievals is reported to be only a few percent over the course of the MetOp-A mission (Tilstra et al., 2012). Other types of degradation can also occur that may or may not cancel in the reflectances. Wavelength shifts and changes in the spectral bandpass can change over time (Dikty et al., 2012). For GOME-2, changes in the instrument bandpass occurred primarily in the ultraviolet (UV) channels of the instrument. Even so, this type of degradation should be handled within the our algorithm with use of the PCA. However, there are still some unexplained instrument behaviors for GOME-2, such as the dependence of the dark signal on temperature (Dikty et al., 2012), that may not be fully accounted for within our algorithm or zero-level adjustment scheme and will lead to systematic errors in SIF retrievals. Various other instrumental effects that may produce false signatures in SCIAMACHY SIF retrievals are documented in Lichtenberg (2006). Their potential impact on SIF retrievals is discussed in Joiner et al. (2012). An approach to mitigate the resulting biases in SIF retrievals is detailed in Sect. 4.4.4.

As compared with pure DOAS retrievals used for trace-gas retrievals, SIF retrievals are more sensitive to the absolute calibration of the solar irradiance data (see Eq. 1). MetOp-A GOME-2 has encountered radiometric degradation over its lifetime. We have made adjustments to the SIF retrievals based on irradiance changes that occurred at 690 nm. We fit a second order polynomial to these irradiances as a function of time after accounting for variations in the sun-Earth distance. These changes are of the order of 15% and occurred primarily over the first 6 years of the mission with stabilization after that.

4.4.2 Cloud filtering and quality control

As detailed in Joiner et al. (2013), we compute an effective cloud fraction f_c. When computing monthly SIF averages, we eliminate data with $f_c > 0.3$. Simulations show that a substantial fraction of the satellite SIF signal can still be detected even through moderately cloudy conditions (Frankenberg et al., 2012). Use of more or less stringent limits on cloud contamination within a moderate range did not substantially alter the derived spatial and temporal patterns of red SIF. However, placing stricter limits decreases the number of samples included in a gridded average. This reduces coverage and increases noise in gridded SIF averages.

In the results shown below, we include all data passing gross quality assurance checks on the retrieval convergence and radiance residuals. These checks typically remove few observations. We also eliminate all data with SZA $> 70°$.

Atmos. Meas. Tech. Discuss., doi:10.5194/amt-2015-387, 2016
Manuscript under review for journal Atmos. Meas. Tech.
Published: 18 January 2016

Atmospheric Measurement Techniques Discussions

4.4.3 Radiance spike removal

The South Atlantic Anomaly (SAA) increases noise in observed radiances, particularly for GOME-2 measurements, in the vicinity of South America over southern Brazil and surrounding areas. In an effort to mitigate the effects of this noise, the following steps are taken. A first step PCA is conducted as outlined above. Then, for each observation, the spectrum is reconstructed using a reduced number of PCs. In this work, we use 20 PCs. The maximum error for each reconstructed spectrum is then computed. Any spectra with maximum errors $> 0.5\%$ are discarded from the sample. The PCA is performed again using only the spectra passing this quality control check. Typically, only a very small fraction of spectra are removed from the sample during this process.

A radiance outlier check is also performed during the retrieval process as follows. A first step retrieval is performed using all radiances within the specified fitting window. Following the retrieval, radiance residuals (observed minus computed from the retrieval) are calculated. If any radiances residuals are $> 0.5\%$, those wavelengths are then given a weight of zero in a second step retrieval. If for a given observation, more than half of the wavelengths have radiance residuals $> 0.5\%$, that observation is flagged. Again, only a very small percentage of spectra are flagged in this process.

4.4.4 Zero-level adjustment

Köhler et al. (2015) found that GOME-2 and SCIAMACHY far-red SIF retrievals exhibited biases, henceforth referred to as zero-level offsets, in the PCA training data set (expected to have a mean near zero) of the order of several tenths of a mW/m^2/nm/sr with systematic dependences on latitude. These biases can be of the same order of magnitude as the SIF signal we are trying to measure. These artifacts result from unaccounted for dark current, stray light, so-called memory effects, and other non-linear responses (e.g. Joiner et al., 2012).

We developed an empirical correction scheme to mitigate zero-level offsets. This scheme is implemented in version 26 GOME-2 data that are publicly available at http://avdc.gsfc.nasa.gov. We use the same correction scheme to adjust red SIF terrestrial retrievals here. The zero-level adjustment scheme is designed to account for instrumental non-linear radiance behavior that appears to slightly distort the spectra as a function of radiance. The scheme may also correct for small effects of rotational-Raman scattering in the atmosphere. As shown below, we find that the biases vary with time (on both daily and monthly time scales) and instrument.

The zero-level adjustment scheme has the following steps 1) Provide a training sample data set of SIF retrievals over ocean passing all quality control checks except the cloud filtering check for a single day; 2) Within a given latitude range, apply a regression model to SIF retrievals in the training data set normalized by incoming clear sky solar irradiance, approximated by SIF/cos(θ), consisting of third order polynomials in θ_0 and continuum radiance; 3) Apply the derived regression coefficients to normalized SIF retrievals over land, then multiply by cos(θ). The regression is not extrapolated beyond the range of radiances and θ_0 values found in the training sample data set. The regression coefficients are generated and applied separately for different latitude bins. For GOME-2 v26 far-red SIF retrievals, we use latitude bins bounded by 90S, 45S, 0, 45N, and 90N. For SCIAMACHY red SIF retrievals, we use latitudes bins bounded by 90S, 0, and 90N and for GOME-2 red SIF retrievals

Atmos. Meas. Tech. Discuss., doi:10.5194/amt-2015-387, 2016
Manuscript under review for journal Atmos. Meas. Tech.
Published: 18 January 2016

90S, 40S, 40N, and 90N. The ranges were chosen empirically to minimize discontinuities at the boundaries and maximize the ability to remove zero-level offsets.

The zero-level adjustment scheme essentially uses ocean data with the assumption of negligible SIF emissions. While this is a good assumption for far-red SIF, there is significant SIF emission in the red SIF region in some areas over ocean as shown below. We did not make any attempt to avoid these areas for the zero-level adjustment scheme. Our regression model assumes that the zero-level adjustment is a smooth function of radiance. As radiance increases from the clear-sky dark to cloudy skies, the ocean SIF signal becomes more shielded. Note that reflectances over land tend to be higher than those over the dark ocean at red wavelengths, so that adjustments over land will typically be made using cloudy ocean data.

We found that after applying the derived regression model over ocean, the spatial patterns of oceanic SIF are still present; this indicates that our regression model has not removed these signals. However, there may be a slight overcorrection in our approach for the red SIF zero-level adjustment. Figure 2 of the supplemental material shows an example of red SIF retrievals for May 2007 with and without zero-level adjustment over both land and ocean. For comparison, we also show high quality oceanic SIF obtained with the full band retrievals that are less susceptible to zero-level offsets. For future versions of the zero-level offset scheme, we intend to explore a two step regression approach whereby we first remove the oceanic SIF signal using full band ocean retrievals before computing regression coefficients. We also have not added barren land to the regression scheme in the present version in order to test how well the scheme works using only cloudy ocean data; the addition of barren land data can easily be accomplished in a future version.

5 Sensitivity analysis

In this section, we retrieve red SIF using the simulation testing data set that contains 230 400 different sets of conditions. Instrument noise is added to the simulated radiances as indicated, where the noise is uncorrelated between channels and follows a Gaussian distribution. The nominal signal to noise ratio (SNR) (referred to as “nom." in Table 1) specified as a function of radiance is similar to that used by Guanter et al. (2015) for GOME-2 and is shown in Fig. 4. Table 1 provides statistics on the differences between the retrievals and the true states for several scenarios described below. To compare true and retrieved SIF, we average SIF over the wavelength range of the red spectral fitting window.

5.1 Sensitivity to number of PCs used

Here, we focus on O_2 band red SIF retrievals with an O_2 B-band fitting window between 682 and 698 nm and for an instrument with FWHM = 0.5 nm and sampling rate of 0.2 nm. The γ band fitting window was 622–640 nm. We use fourth order polynomials to model the surface reflectivity for each fitting window. Use of a higher order polynomial order does not significantly improve the results, while use of a lower order polynomial degrades results.

The first three lines of Table 1 show results for retrievals that use 5, 10, and 15 PCs. There are small biases in all cases with biases generally decreasing with increasing numbers of PCs. The improvement in both accuracy and precision is noticeable when increasing from 5 to 10 PCs and starts to level out with further increases. There is virtually no change in the results when

Atmos. Meas. Tech. Discuss., doi:10.5194/amt-2015-387, 2016
Manuscript under review for journal Atmos. Meas. Tech.
Published: 18 January 2016

Atmospheric Measurement Techniques Discussions

we further increase the number of PCs (not shown). There is a slight bias obtained with both the 10 and 15 PC results as also evidenced by the deviation of the fitted slope from unity. This bias is further discussed below.

We may also compute fluorescence errors using the linear estimation method (Eq. **??**) by assuming random and uncorrelated wavelength-independent radiance errors (as was the case in our simulated data) as in Joiner et al. (2013). However, the linear estimation does not account for errors that may result from using an imperfect model for the SIF spectral emissions or an imperfect forward model (e.g., that does not account explicitly for atmospheric scattering). Here, we have assumed a Gaussian shape for SIF emissions as in Eq. 3. However, interference from far-red emissions in our spectral fitting range slightly distorts the Gaussian shape. We found that it was important to apply some constraint to the SIF emissions spectral shape in order to obtain accurate retrievals, and the Gaussian function provides a reasonable approximation. To accurately evaluate errors resulting from this approach, we show results from the full end-to-end simulation in this work rather than from the linear estimation.

5.2 Sensitivity to the fitting window and instrumental noise

In line 4 of Table 1, we use a smaller O_2 B-band fitting window (682–689 nm) than for results shown in lines 1–3. With this smaller fitting window, we specified $\sigma = 7.5$ in Eq. 3 as compared with $\sigma = 10$ that was used for the larger fitting window. With this configuration, we reduce biases (results are closer to the 1:1 line). This is likely because the assumed Gaussian shape is more applicable to the smaller fitting window. However as expected, the use of a smaller fitting window decreases retrieval precision (σ increases).

Line 5 shows results with the same O_2 B-band fitting window, but now without the benefit of the O_2 γ-band. Removing the γ band decreases precision and increases bias. However, results with no instrument noise (lines 7 and 9) show that precision improves when the γ band is not used. Also in contrast to the results with noisy data, precisions are improved with the smaller O_2 B-band fitting window when noise is absent and the γ band is included. We may therefore infer that the primary benefit of the larger fitting window in the O_2 B-band as well as the addition of the γ band is to beat down the effects of instrumental noise.

In order to assess how much of an impact the solar line filling has on the results, we conducted simulations using a flat solar spectrum and no instrumental noise. Results shown in line 8 of Table 1 indicate that there is a substantial stabilizing effect of the solar line filling for the O_2 band retrievals. Note that solar line filling occurs both inside and outside the O_2 B-band. An additional experiment with a flat solar spectrum and without the γ-band included in the fitting resulted in poor performance with many non-convergent retrievals.

Line 10 shows results for a simulation with two times the nominal noise for the larger B-band fitting window. Errors increased, but less than a factor of 2. This is consistent with the fact that errors are present even without noise, a consequence of small state-dependent errors.

Atmos. Meas. Tech. Discuss., doi:10.5194/amt-2015-387, 2016
Manuscript under review for journal Atmos. Meas. Tech.
Published: 18 January 2016

5.3 Sensitivity to spectral resolution, sampling, and wavelength jitter

We performed simulations for O_2 red SIF retrievals at a higher spectral resolution (FWHM = 0.3 nm, sampling of 0.1 nm) than in the previous simulations. Lines 11–12 of Table 1 show retrieval statistics at the higher spectral resolution with the nominal noise model for fitting windows of 682–698 nm and 682–689 nm, respectively. The precision significantly improves as compared with FWHM = 0.5 nm retrievals. This improvement results from 1) more spectral samples within the fitting window and 2) a larger filling-in signal from SIF in the deepest part of the O_2 B-band as well as within the solar Fraunhofer lines. This is consistent with the simulations of expected FLEX performance for the red SIF (Cogliati et al., 2015).

We also performed simulations for solar line red SIF retrievals using a single small spectral fitting window that contains only solar Fraunhofer lines, similar to those used by Wolanin et al. (2015) and Guanter et al. (2015) (682–686.7 nm, lines 13–16 of Table 1). Here we used the nominal noise model with FWHMs of 0.1, 0.2, 0.3 and 0.5 nm with sampling rates of 0.03, 0.075, 0.1, and 0.2 nm, respectively. When using only solar Fraunhofer lines for the retrieval, a significant improvement is obtained at higher spectral resolutions for the same reasons given above for the O_2 band retrievals. Note that good performance can be achieved with a smaller number of PCs for this limited fitting window. The results obtained at FWHM values of 0.5 and 0.3 nm show that significant improvements are achieved when instrumental noise is simulated and the oxygen B- and γ-bands are included in the spectral fitting as compared with the use of the more limited fitting window that contains only solar lines.

We performed an additional experiment at 0.3 nm spectral resolution where we resampled the spectra at the same spacing as used for 0.5 nm spectral resolution (sampling rate of 0.2 nm). As expected owing to enhanced sensitivity, improvement is obtained at the higher spectral resolution with identical spectral sampling (line 17 of Table 1). This demonstrates the benefits of higher spectral resolution.

Finally, we simulated a random wavelength jitter with a normal distribution and standard deviation of 0.01 nm in both training and testing data sets at 0.3 and 0.5 nm spectral resolutions. Such a jitter may be expected due to changes in the response function with inhomogeneous scenes (e.g., partial clouds). While there is a small degradation in the results, overall the impact of such jitter with our approach is relatively small (lines 18–19 of Table 1 compared with lines 15–16).

5.4 Radiance residuals from simulated data

Figure 5 shows the root-mean-squared (RMS) of the radiance residuals (observed minus calculated radiance) for an instrument with FWHM = 0.5 nm, with nominal noise, and for O_2 band retrievals using B-band fitting window of 682–698 nm when red SIF is and is not retrieved. The displayed values represent the RMS of the residual at each wavelength averaged over all conditions in the simulation testing data as a percentage of the observed radiance. Reductions in the residuals are shown on average when fluorescence is retrieved, as expected. The RMS reductions are not particularly apparent within the O_2 γ band portion of the fitting window where fluorescence is not present. However, reductions are substantial in the O_2 B-band portion of the fitting window, both inside and outside the band. Residuals are reduced outside the B-band ($\lambda < 686.5$ nm) where solar Fraunhofer line filling from SIF occurs. RMS reductions also occur inside the O_2 B-band at wavelengths between 687 and 693 nm. At longer wavelengths ($\lambda > 693$ nm), filling-in of H_2O lines also occurs and some RMS reductions are seen. When

SIF is fit, the radiance residuals are relatively constant with wavelength at a level of around 0.1% or less, consistent with the noise levels in the simulation.

5.5 Discussion of simulation results

As described above and shown in Joiner et al. (2013), there are 60 distinct fluorescence spectra in the testing data set. For each fluorescence spectrum, the simulation contains a number of different observing conditions (e.g., SZAs, VZAs, surface pressures, temperature profiles, and aerosol parameters). Figure 6 shows results for O_2 band (smaller fitting window) and solar line retrievals with FWHM = 0.5 nm and nominal noise. This figure shows that negative biases are more prevalent for the O_2 band retrievals at higher levels of fluorescence and for certain simulation configurations. However, the improvement in terms of precision obtained with the O_2 band retrievals as compared with the solar line approach is also apparent. This implies that reasonable red SIF retrievals should be obtained using our new approach with existing instruments (provided they behave as expected) and that higher spectral resolution is not an absolute necessity for red SIF retrievals so long as both the O_2 γ and B-bands are available.

Our retrieval approach relies on several simplifying assumptions, such as that the geometrical air mass factor is an appropriate approximation and that the spectral structures of SIF and ρ_s can be modeled reasonably well with a few parameters. The simulated data do not contain these assumptions; the radiances are generated monochromatically with atmospheric scattering before being convolved with the instrument response function, and the spectral dependences of SIF and ρ_s are based on model and spectral libraries. Therefore, our simulation results should accurately reflect errors produced by our assumptions. As can be seen, the biases and errors produced by these simplifications are relatively small. Our simulation results provide confidence that our method can be used to successfully retrieve red SIF with satellite measurements from GOME-2 and SCIAMACHY provided that the instruments are performing in a linear and expected manner and that remaining biases can be effectively removed.

6 Results from GOME-2 and SCIAMACHY data

For GOME-2 and SCIAMACHY O_2 red SIF retrievals, we use a fitting window of 682–692 nm and 15 PCs. Although we obtain good results using simulated data that include wavelengths impacted by H_2O (vapor) absorption ($692 < \lambda < 713$ nm), we found unrealistic month-to-month variations in both far-red and red SIF magnitudes with real satellite data when using wavelengths impacted by H_2O absorption. These unphysical variations were drastically reduced when we restricted the retrievals to wavelengths with minimal H_2O absorption. Use of the 682–692 nm window was chosen to maximize wavelength range in order to minimize the impact of instrumental random noise while minimizing the impact of H_2O absorption. Similarly, in version 26 of far-red GOME-2 SIF retrievals we restricted the fitting window to 734–758 nm, a reduction as compared with that used in Joiner et al. (2013). This also reduced unrealistic month-to-month variations that were present in earlier versions. For solar line red SIF retrievals, we use a window of 682–686.5 nm with 3 PCs. This is slightly larger than the fitting window used by Wolanin et al. (2015) (681.8–685.5 nm).

Atmos. Meas. Tech. Discuss., doi:10.5194/amt-2015-387, 2016
Manuscript under review for journal Atmos. Meas. Tech.
Published: 18 January 2016

Atmospheric Measurement Techniques Discussions

6.1 Radiance residuals from GOME-2

Figure 7 is similar to Fig. 5 but shows the spectral RMS of GOME-2 radiance residuals, obtained with and without fitting SIF. The residuals shown here were obtained on a single day (01 July 2007) and are averaged for each wavelength over all observations with SZA $< 70°$ and the Normalized Difference Vegetation Index (NDVI) > 0.5 (i.e., moderately to highly vegetated pixels) that passed quality control and cloud filtering checks. Reductions in the residuals are modest and smaller than those obtained using the simulated data in Fig. 5. As will be shown below, we retrieve values of red SIF with GOME-2 and SCIAMACHY that are on average lower than those present in the simulation data set. We should therefore expect smaller reductions in residuals when SIF is fit with the GOME-2 data as compared with the simulated data. The largest reductions are in the solar Fraunhofer lines near 684 nm and within the deepest part of O_2 B-band around 687-690 nm. Overall, RMS residuals have similar or slightly smaller magnitudes as compared with those shown in Fig. 5 for simulated data. This indicates that the noise model used in our simulations is appropriate for GOME-2. We note somewhat better performance of GOME-2 in the O_2 γ-band spectral region as compared with that near the B-band.

6.2 Comparison of GOME-2 and SCIAMACHY red SIF

Global composites of red SIF derived from SCIAMACHY and GOME-2 for July and December 2009 are displayed in Fig. 8. For comparison, these are the same months displayed in Wolanin et al. (2015). Quality-filtered retrievals have been averaged in 1° latitude-longitude grid boxes in all cases. The filtering uses data only for SZA$< 70°$, where RRS effects should be relatively small (Joiner et al., 2012). A zero-level adjustment is made as described above for all cases. No other explicit account of rotational-Raman scattering is made.

The top panels show retrievals obtained using the solar line approach with a fitting window of 682–686.5 nm for SCIAMACHY. The fitting window is similar to that used by Wolanin et al. (2015). The main difference of our approach as compared with that used by Wolanin et al. (2015) here is that we use the PCA approach to account for H_2O absorption and our zero-level offset adjustment may account for the effects of RRS as well as other instrumental artifacts. Magnitudes are similar but perhaps slightly higher than those shown in Wolanin et al. (2015). Here, we display results over all land areas that meet our filtering criteria. Note that retrievals in many areas such as deserts and the Himalayan plateau were not shown in Wolanin et al. (2015) so that we are unable to compare results there.

Unrealistic high biases are seen over the Sahara and Arabian peninsula in July and to a lesser extent in December. These are cases of high surface reflectance and small amounts of vegetation. A simple filter for high reflectivities (> 0.35) can remove these cases or alternatively they could be used in the training data set for the zero-level offset adjustment scheme. However, to examine potential instrumental effects and our ability to remove them, we have not filtered the data or included them in the zero-level offset regression training. Similar biases in SCIAMACHY data at the deep Ca II line at 866 nm were also discussed in Joiner et al. (2012). Zero-level adjustments are typically of the order of a few tenths of a mW/m^2/nm/sr. The adjustments do not completely remove biases at high radiance levels as shown here.

The middle and bottom panels show red SIF retrievals obtained using the O_2 band retrievals with SCIAMACHY and GOME-2, respectively. A generally good agreement of the SIF magnitudes and spatial patterns is observed between the satellite retrievals obtained with different instruments and fitting windows. High red SIF values are observed over vegetated areas, while low (or sometimes negative) values are obtained over deserts and sparsely vegetated areas. Spatial patterns of active regions are similar to those of far-red SIF retrievals (740–770 nm) obtained by GOME-2 and GOSAT. Values of red SIF are generally lower than those obtained in the far-red consistent with previous canopy-level ground-based measurements (Daumard et al., 2010; Cheng et al., 2013; Fournier et al., 2012).

Positive biases over bright desert areas are less prevalent in the O_2 band retrievals, particularly for SCIAMACHY. However, some biases are seen in the GOME-2 retrievals in December. Again, these can be removed with a simple high reflectance filter. We also note that there are larger negative biases over non-vegetated areas obtained with SCIAMACHY as compared with GOME-2. The fact that similar results are obtained over vegetated areas suggests that the instruments are behaving differently over high reflectivity scenes. There are other differences between the retrievals even in vegetated areas. In the case where identical algorithms are applied, these differences are likely instrument related and will be explored in more detail below.

We note that biases (both before and after zero-level adjustment) vary over time. Figure 1 in the supplemental material shows similar results obtained in 2007. The unphysical high biases over the Sahara are much reduced for the solar line retrievals in July 2007 as compared with July 2009 and similarly for the GOME-2 O_2 band retrievals in Dec. 2007 as compared with 2009. It should be noted again that these red SIF retrievals are derived using instruments that were not designed or optimized for such measurements.

6.3 Variability, biases, and estimated errors in GOME-2 and SCIAMACHY red SIF retrievals

Standard deviations of the July 2007 red SIF retrievals in the left panels of Fig. 9 show the variability of the retrieved red SIF in $1^\circ \times 1^\circ$ grid boxes for the three different retrievals in Fig. 8. This variability results from the effects of instrumental noise, natural variability in vegetation activity within the month, cloud effects, the effects of different illumination and viewing geometries, and the different footprints from the satellite orbits. SCIAMACHY retrievals show less variability in general as compared with GOME-2, particularly in the area impacted by the SAA (high variability over parts of South America). This indicates a better performance per pixel of the SCIAMACHY instrument in the red spectral region. Lower variability is shown for the SCIAMACHY O_2 retrievals as compared with the solar line retrievals as may be expected from the use of additional spectral range.

In general for both instruments, higher standard deviations occur over brighter scenes (e.g., over Greenland and deserts) consistent with the higher noise expected at higher radiance levels. Interestingly, vegetation patterns are not obvious in the standard deviation maps, indicating that there is not much additional variability contributed by vegetation as compared with that from instrumental noise. This was not the case for far-red retrievals from GOME-2 and SCIAMACHY (Joiner et al., 2013; Köhler et al., 2015). Variability due to noise (in radiance units) in sparsely vegetated areas is higher for GOME-2 in the red as compared with the far-red shown in Joiner et al. (2013). Variability in vegetated areas is similar.

The right panels of Fig. 9 show computed standard errors of the monthly mean (grid box standard deviations divided by the square root of the number of retrievals). Despite lower variability in the SCIAMACHY solar line red SIF retrievals, the GOME-2 retrievals show lower standard errors than SCIAMACHY solar line retrievals in all but a few areas owing to more observations per month. The SCIAMACHY O_2 band red SIF retrievals provide slightly lower standard errors in most areas as compared with those of GOME-2. However, there is some block-like structure in the SCIAMACHY standard errors. The block-like structure results from alternating blocks of nadir and limb retrievals that were performed by SCIAMACHY. GOME-2 operates exclusively in the nadir mode.

Figure 10 shows monthly mean zero-level offset adjustments for July and December 2007 for the three red SIF retrievals. Both SCIAMACHY retrievals show positive and negative adjustments while GOME-2 shows mostly negative adjustments. SCIAMACHY adjustments for the O_2 band red SIF retrievals show alternating blocky spatial patterns; this results from day to day variation in the estimated zero-level adjustments. Adjustments for the two SCIAMACHY retrievals are different because they are using different retrieval approaches and fitting windows. The O_2 B-band is a deeper feature than the solar lines and may therefore behave differently. RRS increases rapidly with solar zenith angle at high solar zenith angles (Joiner et al., 2012). The zero level adjustments do not clearly or consistently show this effect.

As can be seen, the zero-level adjustments are substantial in many areas. Uncertainties in the zero-level adjustment likely dominate the retrieval errors. The day-to-day and even at times orbit to orbit variation in the SCIAMACHY offsets lead to larger uncertainties than for GOME-2. Note that there are some some discontinuities at the latitudes where the boundaries for the adjustments are defined. However, they are not very pronounced in the figures. The latitude dependences of the zero-level biases shown here are roughly consistent in terms of latitudinal dependence with those found by Köhler et al. (2015) for SCIAMACHY and GOME-2 far-red solar line retrievals. Based on the magnitude and stability of the adjustments, we estimate that uncertainties in monthly mean red SIF retrievals are in the range 0.1–0.3 mW/m^2/nm/sr for SCIAMACHY data and 0.1–0.2 mW/m^2/nm/sr for GOME-2 O_2 band retrievals.

6.4 Time series and mapped anomalies

We display time series of red and far-red SIF for the boxes shown in Figure 11. Each box is an average over an area of 3° latitude by 3° longitude. Figure 12 shows that red and far-red SIF display similar seasonality. Many of the boxes shown also display a fair amount of inter-annual variability (IAV). The IAV is similar for red and far-red SIF and in the areas shown is driven primarily by water availability. Yoshida et al. (2015) and Sun et al. (2015) showed that drought-related negative SIF anomalies (e.g., the 2011 low values shown for Box 1 in the Texas drought area) are driven by decreases in the fraction of photosynthetically-active radiation (fPAR) as well as decreases in fluorescence efficiency that is related to electron transport rate within leaves. There is a somewhat earlier autumn or dry season decline in the far-red SIF as compared with the red in some of the boxes (1 and 2). The seasonality of far-red SIF has been shown to closely match that of gross primary productivity (GPP) derived from flux tower eddy covariance measurements while greenness vegetation indices that are related to fPAR tended to decline later in autumn (Joiner et al., 2014).

To further assess the GOME-2 red SIF data set, we compute monthly mean anomalies and compare with those from the far-red. We should expect to see some similarities in the anomalies, particularly those driven by moisture stress (e.g., Daumard et al., 2010; Ač et al., 2015; Middleton et al., 2015). Showing consistency (or not) in the anomalies demonstrates the ability to resolve small signals and therefore provides a check on the estimated errors and sensitivities.

Figure 13 shows mapped gridded monthly anomalies for far-red and red SIF from GOME-2 for August 2010, 2011, and 2012. These months highlight the impact of droughts where SIF satellite observations have been studied previously (Yoshida et al., 2015; Sun et al., 2015; Lee et al., 2013). To generate the anomalies, monthly mean climatological maps averaged over the years between 2007 and 2014 are subtracted from the monthly mean fields. The anomalies are then shown as a fraction of the climatological gridbox value for a particular month. Far-red SIF anomalies are gridded at a resolution of 0.5° resolution. To reduce the impact of retrieval noise, red SIF anomalies are shown at a resolution of 1°. Data are shown for gridboxes where the climatological NDVI from GOME-2 > 0.2.

Negative anomalies due to the Russian drought of 2010 are clearly shown in both red and far-red SIF anomaly maps while at the same time positive anomalies are shown in the western US and northeast Mexico. Smaller negative anomalies are also shown in southern Amazonia in 2010 and may be the result of the drought conditions (Lewis et al., 2011). Shown in terms of a percent of the monthly mean climatological values, the anomalies appear to be somewhat larger in the red SIF as compared with the far-red. However, the differences may be within the uncertainties of the zero-level adjustment scheme.

Negative SIF anomalies due to the Texas drought of 2011 are also shown in both red and far-red SIF in Texas and northern Mexico, while mostly positive anomalies are shown in the Russian grain belt during this year. Similarly, negative far-red and red SIF anomalies are shown in the region of the 2012 US great plains drought in the western US. Spatial patterns of red and far-red anomalies are consistent elsewhere such as just to the south of the Sahara and to the east of the Gobi desert.

Figure 14 shows time series of monthly anomalies (absolute magnitudes in radiance units, not fractional values) for boxes from Fig. 11. Overall, the temporal dependence of the anomalies is very similar, at least to within the uncertainties of the measurements. This demonstrates the ability of the GOME-2 monthly red SIF at the box resolution to resolve signals of the order of +/-0.1 mw/m^2/nm/sr. Expected future work includes a closer examination of the anomalies.

6.5 Oceanic SIF retrievals

Oceanic red SIF can be retrieved using the filling-in of solar Fraunhofer lines (Wolanin et al., 2015), the continuum emission above the dark ocean surface (Hu et al., 2005), or both, as shown here. Here, we retrieve oceanic fluorescence line height (FLH) with GOME-2 and SCIAMACHY using the method discussed above. Use of the large fitting window encompassing the red SIF emission feature is not only feasible for oceanic FLH retrievals, owing to the otherwise relatively dark ocean surface, but also beneficial. Firstly, fitting the peak as well as both shoulders of the red SIF emission feature allows for a clean separation of its spectral structure with that of water leaving radiance, atmospheric scattering and absorption, and Raman scattering in both the ocean and atmosphere. Secondly, use of this large fitting window also reduces the impact of instrumental noise and other artifacts such as non-linearity effects that impact the small radiance levels typically measured over ocean. No further zero-level adjustments were made to the oceanic retrievals as was done for the terrestrial red SIF retrievals.

Our results from SCIAMACHY and GOME-2, shown in Fig. 15, compare well with each other and with the simpler three broadband channel approach applied to the Terra MODIS (Aqua MODIS results, not shown, were similar, but we show Terra data here as the local overpass times are more similar to those of Envisat and MetOp). MODIS data, provided at a spatial resolution of 9 km, were downloaded from http://oceandata.sci.gsfc.nasa.gov. GOME-2 provides superior sampling as compared with SCIAMACHY as it operates in nadir mode exclusively. In Fig. 15 we display GOME-2 data gridded at a 0.5° spatial resolution. SCIAMACHY, which alternated between limb and nadir mode observations, is gridded at a resolution of 1° so as not to show too many gaps between grid boxes. Results from GOME-2 and SCIAMACHY, using the full wavelength range between 660 and 713 nm, are less noisy than those obtained by Wolanin et al. (2015) with a smaller fitting window that includes only solar Fraunhofer lines.

Here, we apply a very simple adjustment to provide normalized fluorescence line height (nFLH, normalized with respect to incoming solar irradiance) to facilitate comparisons with MODIS nFLH. Our approach accounts only for $\cos(\theta)$ (i.e., it does not account for the effects of atmospheric scattering and absorption or changes in the sun-Earth distance). Nevertheless, the agreement with MODIS in terms of the magnitude and spatial patterns, is excellent. We note that our results are referenced to 683 nm while MODIS uses slightly different wavelengths so that our magnitudes are expected to be somewhat higher as is generally shown. Finally, it should be noted that a more liberal cloud filter is applied to the GOME-2 and SCIAMACHY retrievals as compared with that used for MODIS, particularly considering that MODIS has a much smaller footprint (of the order of 1 km^2).

Figure 16 shows the mean spectral residuals with and without fitting ocean fluorescence for GOME-2 on 01 July 2007. The reduction in residuals supports that most of the information in fitting for ocean FLH is coming from the broad SIF continuum emission as opposed to filling-in of telluric or solar lines.

7 Conclusions

We have developed new approaches to retrieve SIF at red wavelengths over land from moderate spectral resolution satellite instruments. We also showed for the first time that red SIF can be retrieved over ocean with good fidelity with the same instruments by utilizing the full wavelength range of the SIF emission. Similar to previous works, we use use a principal component analysis (PCA) approach to estimate the spectral structure of atmospheric absorption. Our PCA approach utilizes the O_2 γ band, which is relatively free of SIF, as well as the filling-in of solar Fraunhofer lines to help anchor the O_2 B-band that is used to increase the precision of SIF retrievals. A simplified radiative transfer model based on the geometrical air mass factor approximation is used to determine how much of the emitted surface SIF signal is absorbed in the atmosphere.

We used simulated data computed with a full radiative transfer model for thousands of different scenarios to demonstrate that high quality red SIF retrievals can be obtained using satellite instrumentation with a relatively high SNR and moderate spectral resolution similar to GOME-2 and SCIAMACHY. Retrieval errors depend upon the instrument SNR, the spectral fitting window used, and spectral resolution. We demonstrate that use of the O_2 γ- and B-bands can increase red SIF retrieval precision as compared with approaches that utilize a smaller fitting window confined to regions outside the O_2 B-band where the SIF signal is obtained solely by filling in of solar Fraunhofer features.

We applied our new approach to satellite measurements from GOME-2 and SCIAMACHY. The GOME-2 and SCIAMACHY retrievals that use the O_2 γ- and B-bands compare well with those from SCIAMACHY that use the less complex and also less sensitive solar line filling narrow window approach. Red SIF uncertainties for monthly mean gridded data are estimated to be ∼0.1–0.3 mW/m^2/nm/sr and are a consequence of both random and systematic errors. Our long time series of red SIF from GOME-2 allows for the calculation of globally mapped monthly mean anomalies. These first maps of red SIF anomalies show similar temporal and spatial patterns as compared with far-red SIF anomalies though with somewhat larger fractional values.

Several satellite instruments with red spectral coverage and various spectral and spatial resolutions have flown, are currently flying, or are planned for launch in the next few years. The approach outlined here can potentially be applied to these instruments. The original GOME instrument, launched in 1995 on the ESA European Remote Sensing satellite 2 (ERS-2), can also be used for red SIF measurements, but with a larger pixel size (40 km × 320 km) in its nominal operating mode. GOME has the unique ability to extend the record of SIF measurements back to 1995. In the future, the approach developed here may be applied to the US National Aeronautics and Space Administration (NASA) Earth Ventures 1 Tropospheric Emissions: Monitoring of Pollution (TEMPO) (Chance et al., 2013), a geostationary instrument designed primarily for air quality measurements planned for launched near the end of the decade. TEMPO should provide the first hourly terrestrial red SIF measurements throughout the day with coverage over much of the populated areas of North America and as well as oceanic SIF over surrounding coastlines. With nearly continuous spectral coverage from the ultraviolet through approximately 740 nm and a spectral resolution of ∼0.6 nm, it should obtain time-resolved far-red as well as red SIF retrievals at a substantially higher spatial resolution (native ground pixel of 2 km by 4.5 km at the center of the field of regard) than GOME-2 or SCIAMACHY. The FLuorescence EXplorer (FLEX) (ESA, 2015), a selected ESA Earth Explorer 8 Mission, plans to utilize the O_2 A- and B-bands for SIF retrievals (Guanter et al., 2010; Cogliati et al., 2015) and other bio-spectral information across the visible-NIR spectrum. FLEX will provide measurements at an even higher spatial resolution (∼300 m) at approximately a monthly time scale.

Acknowledgements. Funding for this work was provided by the Emmy Noether Programme (GlobFluo project) of the German Research Foundation. The authors are indebted to Phil Durbin, Ghassan Taha, and Michael Yan, for assistance with the satellite data sets. We gratefully acknowledge the European Meteorological Satellite (EUMetSat) program, ESA, and NASA, particularly the MODIS data processing team, for making available the GOME-2, SCIAMACHY, and MODIS data used here. We also thank Karl (Fred) Huemmrich, William Cook, Qingyuan Zhang, Rose Munro, Rüdiger Lang, Joseph Berry, John Burrows, P. K. Bhartia, Petya Campbell, Lawrence Corp, Kelly Chance, and Arlindo da Silva for helpful discussions.

References

Abbott, M. R., and Letelier, R. M.: Algorithm theoretical basis document chlorophyll fluorescence, Available at http://www.modis.gsfc.nasa.gov/data/atbd, 1999.

Ač, A., Malenovsky, Z., Olejničková, J., Gallé, A., Rascher, U., and Mohammed, G.: Meta-analysis assessing potential of steady-state chlorophyll fluorescence for remote sensing detection of plant water, temperature and nitrogen stress, Rem. Sens. Environ., 168, 420–436, doi:10.1016/j.rse.2015.07.022, 2015.

Agati, G., Mazzinghi, P., Fusi, F., and Ambrosini, I.: The f685/f730 chlorophyll fluorescence ratio as a tool in plant physiology - response to physiological and environmental-factors, J. Plant Physiol., 145, 228-238, 1995.

Agati, G., Mazzinghi, P., diPaola, M. L., Fusi, F., and Cecchi, G.: The F685/F730 chlorophyll fluorescence ratio as indicator of chilling stress in plants, J. Plant Physiol., 148, 384-390, 1996.

Agati, G., Cerovic, Z. G., and Moya, I.: The effect of decreasing temperature up to chilling values on the in vivo f685/f735 chlorophyll fluorescence ratio in phaseolus vulgaris and pisum sativum: the role of the photosystem I contribution to the 735 nm fluorescence band, Photochem. Photobiol., 72, 75-84, 2000.

Behrenfeld, M. J., Westberry, T. K., Boss, E. S., O'Malley, R. T., Siegel, D. A., Wiggert, J. D., Franz, B. A., McClain, C. R., Feldman, G. C., Doney, S. C., Moore, J. K., Dall'Olmo, G., Milligan, A. J., Lima, I., and Mahowald, N.: Satellite-detected fluorescence reveals global physiology of ocean phytoplankton, Biogeosci., 6, 779-794, doi:10.5194/bg-6-779-2009, 2009.

Campbell, P. K. E., Middleton, E. M., McMurtrey, J. E., Corp, L. A., and Chappelle, E. W.: Assessment of vegetation stress using reflectance or fluorescence measurements, J. Environ. Qual., 36, 832-845, 2007.

Campbell, P. K. E., Middleton, E. M., Corp, L. A., and Kim, M. S.: Contribution of chlorophyll fluorescence to the apparent vegetation reflectance, Sci. Total Environ., 404, 433–439, 2008.

Chance, K., Liu, X., Suleiman, R., Flittner, D., Al-Saadi, J., Janz, S., Status of the first NASA EV-I project, Tropospheric Emissions: Monitoring of Pollution (TEMPO), AGU Fall Meeting Presentation A43I-01, http://www.cfa.harvard.edu/atmosphere/publications.html, 2013.

Cheng, Y.-B., Middleton, E. M., Zhang, Q., Huemmrich, K. F., Campbell, P. K., Cook, B. D., Kustas, W. P., and Daughtry, C. S.: Integrating solar induced fluorescence and the photochemical reflectance index for estimating gross primary production in a cornfield, Remote Sens., 5, 6857-6879, 2013.

Corp, L. A., McMurtrey, J. E., Middleton, E. M., Mulchi, C. L., Chappelle, E. W., and Daughtry, C. S. T.: Fluorescence sensing systems: in vivo detection of biophysical variations in field corn due to nitrogen supply, Remote Sens. Environ., 86, 470–479, 2003.

Corp, L. A., Middleton, E. M., McMurtrey, J. E., Campbell, P. K. E., and Butcher, L. M.: Fluorescence sensing techniques for vegetation assessment, Appl. Optics, 45, 1023–1033, 2006.

Corp, L.A., Middleton, E. M., Campbell, P. K. E., Huemmrich, K. F., Cheng, Y. B., and Daughtry, C. S. T.: Spectral indices to monitor nitrogen driven carbon uptake in field corn, J. Appl. Remote Sens., 4, 0435555, doi:10.1117/1.3518455, 2010.

Callies, C., Corpaccioli, E., Eisinger, M., Hahne, A., and Lefebvre, A.: GOME-2 – MetOp's Second-Generation Sensor for Operational Ozone Monitoring, available at: http://esamultimedia.esa.int/docs/metop/GOME-2-102.pdf (last access: 13 April 2013), ESA Bull.-Eur. Space, 103, 28–36, 2000.

Cogliati, S., Verhoef, W., Kraft, S., Sabater, N., Alonso, L., Vicent, J., Moreno, J., Drusch, M., and Colombo, R.: Retrieval of sun-induced fluorescence using advanced spectral fitting methods, Rem. Sens. Environ., 169, 344-357, 2015.

Daumard, F., Champagne, S., Fournier, A., Goulas, Y., Ounis, A., Hanocq, J.-F., and Moya, I.: A field platform for continuous measurement of canopy fluorescence, IEEE Trans. Geosci. Remote., 48, 3358–3368, 2010.

Dikty, S., Richer, A., Weber, M., Noël, S., Bovensmann, H., Wittrock, F., and Burrows, J. P.: GOME-2 on MetOp-A support for analysis of GOME-2 in-orbit degradation and impacts on level 2 data products, Final Report, Univ. Bremen, http://www.iup.uni-bremen.de/doas/reports, 2012.

ESA: Report for Mission Selection: FLEX, ESA SP-1330/2 (2 volume series), European Space Agency (ESA), 197pp., Noordwijk, The Netherlands, 2015.

Fell, F. and Fischer, J.: Numerical simulation of the light field in the atmosphere–ocean system using the matrix–operator method, J. Quant. Spectrosc. Rad. Trans., 69, 351–388, 2001.

Fournier, A., Daumard, F., Champagne, S., Ounis, A., Goulas, Y., and Moya, I.: Effect of canopy structure on sun-induced chlorophyll fluorescence, ISPRS J. Photogramm., 68, 112–120, doi: 10.1016/j.isprsjprs.2012.01.003, 2012.

Frankenberg, C., Butz, A., and Toon, G. C.: Disentangling chlorophyll fluorescence from atmospheric scattering effects in O_2 A-band spectra of reflected sun-light, Geophys. Res. Lett., 38, L03801, doi: 10.1029/2010GL045896, 2011a.

Frankenberg, C., Fisher, J. B., Worden, J., Badgley, G., Saatchi, S. S., Lee, J.-E., Toon, G. C., Butz, A., Jung, M., Kuze, A., and Yokota, T.: New global observations of the terrestrial carbon cycle from GOSAT: patterns of plant fluorescence with gross primary productivity, Geophys. Res. Lett., 38, L17706, doi:10.1029/2011GL048738, 2011b.

Frankenberg, C., O'Dell, C., Guanter, L., and McDuffie, J.: Remote sensing of near-infrared chlorophyll fluorescence from space in scattering atmospheres: implications for its retrieval and interferences with atmospheric CO_2 retrievals, Atmos. Meas. Tech., 5, 2081–2094, doi: 10.5194/amt-5-2081-2012, 2012.

Frankenberg, C., O'Dell, C., Berry, J., Guanter, L., Joiner, J., K/'ohler, P., Pollack, R., and Taylor, T. E.: Prospects for chlorophyll fluorescence remote sensing from the Orbiting Carbon Observatory-2, Remote Sens. Environ., 147, 1-12, 2014.

Gitelson, A. A., Buschmann, C., and Lichtenthaler, H. K.: Leaf chlorophyll fluorescence corrected for re-absorption by means of absorption and reflectance measurements, J. Plant Phys., 152, 283–296, 1998.

Gower, J. F. R., and King, S.: Validation of chlorophyll fluorescence derived from MERIS on the west coast of Canada, Intl. J. Remote Sens., 28, 625–635, 2007.

Gower, J. F. R., and King, S.: Use of satellite images of chlorophyll fluorescence to monitor the spring bloom in coastal waters, Intl. J. Rem. Sens., 33, 7469–7481, 2012.

Gower, J. F. R.: On the use of satellite-measured chlorophyll fluorescence for monitoring coastal waters, Intl. J. Rem. Sens., doi:10.1080/01431161.2015.1111542, 2015.

Guan, K., Pan, M., Li, H. Wolf, A., Wu, J., Medvigy, D., Caylor, K. K., Sheffield, J., Wood, E. F., Malhi, Y., Liang, M., Kimball, J. S., Saleska, S. R., Berry, J., Joiner, J., Lyapustin, A. I.: Photosynthetic seasonality of global tropical forests controlled by hydroclimate, Nature Geosci., doi:10.1038/ngeo2382, 2015a.

Guan, K., Berry, J., Zhang, Y., Joiner, J., Guanter, L., Badgley, G., Lobell, D. B., 2015: Improving the monitoring of crop productivity using spaceborne solar-induced fluorescence, Global Change Biol., doi: 10.1111/gcb.13136, 2015b.

Guanter, L., Alonso, L., Gómez-Chova, L., Amorós-López, J., Vila-Francés, J., and Moreno, J.: Estimation of solar-induced vegetation fluorescence from space measurements, Geophys. Res. Lett., 34, L08401, doi:10.1029/2007GL029289, 2007.

Guanter, L., Alonso, L., Gómez-Chova, L., Meroni, M., Preusker, R., Fischer, J., and Moreno, J.: Developments for vegetation fluorescence retrieval from spaceborne high-resolution spectrometry in the O_2 A and O_2-B absorption bands, J. Geophys. Res., 115, D19303, doi:10.1029/2009JD013716, 2010.

Guanter, L., Frankenberg, C., Dudhia, A., Lewis, P. E., Gómez-Dans, J., Kuze, A., Suto, H., and Grainger, R. G.: Retrieval and global assessment of terrestrial chlorophyll fluorescence from GOSAT space measurements, Remote Sens. Environ., 121, 236–251, 2012.

Guanter, L., Rossini, M., Colombo, R., Meroni, M., Frankenberg, C., Lee, J.-E., and Joiner, J.: Using field spectroscopy to assess the potential of statistical approaches for the retrieval of sun-induced chlorophyll fluorescence from space, Remote Sens. Environ., 133, 52–61, 2013.

Guanter, L., Zhang, Y., Yung, M., Joiner, J., Voigt, M., Berry, J. A., Frankenberg, C., Huete, A. R., Zarco-Tejada, P. Lee, J.-E., Moran, M. S., Ponce-Campos, G., Beer,C., Camps-Valls, G., Buchmann, N., Gianelle, D., Klumpp, K., Cescatti, A., Baker, J. M., Griffis, T. J.: Global and time-resolved monitoring of crop photosynthesis with chlorophyll fluorescence, Proc. Natl. Acad. Sci., 111, E1327–E1333, doi: 10.1073/ pnas.1320008111, 2014.

Guanter, L., Aben, I., Tol, P., Krijger, J. M., Hollstein, A., Köhler, P., Damm, A., Joiner, J., Frankenberg, C., and Landgraf, J.: Potential of the TROPOspheric Monitoring Instrument (TROPOMI) onboard the Sentinel-5 Precursor for the monitoring of terrestrial chlorophyll fluorescence, Atmos. Meas. Tech., 8, 1337-1352, doi:10.5194/amt-8-1337-2015, 2015.

Hu, C., Muller-Karger, F. E., Taylor, C., Carder, K. L., Kelble, C., Johns, E., and Heil, C. A.: Red tide detection and tracing using MODIS fluorescence data: A regional example in SW Florida coastal waters, Remote Sens. Environ., 97, 311-321, doi:10.1016/j.rse.2005.05.013, 2005.

Joiner, J., Yoshida, Y., Vasilkov, A. P., Yoshida, Y., Corp, L. A., and Middleton, E. M.: First observations of global and seasonal terrestrial chlorophyll fluorescence from space, Biogeosci., 8, 637–651, doi: 10.5194/bg-8-637-2011, 2011.

Joiner, J., Yoshida, Y., Vasilkov, A. P., Middleton, E. M., Campbell, P. K. E., Yoshida, Y., Kuze, A., and Corp, L. A.: Filling-in of near-infrared solar lines by terrestrial fluorescence and other geophysical effects: simulations and space-based observations from SCIAMACHY and GOSAT, Atmos. Meas. Tech., 5, 809–829, doi: 10.5194/amt-5-809-2012, 2012.

Joiner, J., Guanter, L., Lindstrot, R., Voigt, M., Vasilkov, A. P., Middleton, E. M., Huemmrich, K. F., Yoshida, Y., and Frankenberg, C.: Global monitoring of terrestrial chlorophyll fluorescence from moderate spectral resolution near-Infrared satellite measurements: Methodology, simulations, and application to GOME-2, Atmos. Meas. Tech., 6, 2803-2823, doi:10.5194/amt-6-2803-2013, 2013.

Joiner, J., Yoshida, Y., Vasilkov, A. P., Schaefer, K., Jung, M., Guanter, L., Zhang, Y., Garrity, S., Middleton, E. M., Huemmrich, K. F., Gu, L., Belelli Machesini, L.: The seasonal cycle of satellite chlorophyll observations and its relationship to vegetation phenology and ecosystem-atmosphere carbon exchange, Remote Sens. Environ., 152, 375-391, doi:10.1016/j.rse.2014.06.022, 2014.

Köhler, P., Guanter, L., and Joiner, J.: A linear method for the retrieval of sun-induced chlorophyll fluorescence from GOME-2 and SCIAMACHY data, Atmos. Meas. Tech., 8, 2589-2608, doi: 10.5194/amt-8-2589-2015, 2015.

Lee, J.-E., Frankenberg, C., van der Tol, C., Berry, J. A., Guanter, L., Boyce, C. K., Fisher, J. B., Morrow, E., Worden, J. R., Asefi, S., Badgley, G., and Saatchi, S.: Amazonian productivity to seasonal water stress: observations from GOSAT chlorophyll fluorescence, Proc. Roy. Soc. B, 280, 20130171, doi:10.1098/ rspb.2013.0171, 2013.

Lee, J.-E., Berry, J. A., van der Tol, C., Yang, X., Guanter, L., Damm, A., Baker, I., and Frankenberg, C.: Simulations of chlorophyll fluorescence incorporated into the Community Land Model version 4, Glob. Change Biol., 21, 3469–3477, doi: 10.1111/gcb.12948, 2015.

Lewis, S. L., Brando, P. M., Phillips, O. L., van der Heijden, G. M. F., and Nepstad, D. C.: The 2010 Amazon Drought, Science, 331, 554–554, doi:10.1126/science.1200807, 2011.

Li, C., Joiner, J., Krotkov, N. A., and Bhartia, P. K.: A fast and sensitive new satellite SO_2 retrieval algorithm based on principal component analysis: Application to the ozone monitoring instrument, Geophys. Res. Lett., 40, 1-5, doi:10.1002/2013GL058134, 2013.

Li, C., Joiner, J., Krotkov, N. A., and Dunlap, L.: A new method for global retrievals of HCHO total columns from the Suomi National Polar-orbiting Partnership Ozone Monitoring and Profiler Suite, Geophys. Res. Lett., 42, doi: 10.1002/2015GL063204, 2015.

Lichtenberg, G., Kleipool, Q., Krijger, J. M., van Soest, G., van Hees, R., Tilstra, L. G., Acarreta, J. R., Aben, I., Ahlers, B., Bovensmann, H., Chance, K., Gloudemans, A. M. S., Hoogeveen, R. W. M., Jongma, R. T. N., Noël, S., Piters, A., Schrijver, H., Schrijvers, C., Sioris, C. E., Skupin, J., Slijkhuis, S., Stammes, P., and Wuttke, M.: SCIAMACHY Level 1 data: calibration concept and in-flight calibration, Atmos. Chem. Phys., 6, 5347?5367, doi:10.5194/acp-6-5347-2006, 2006.

Lichtenthaler, H. K.: Chlorophyll fluorescence signatures of leaves during the autumnal chlorophyll breakdown, J. Plant Physiol., 131, 101–110, 1987.

Lichtenthaler, H. K.: Applications of chlorophyll fluorescence in photosynthesis research, stress physiology, hydrology and remote sensing, Kluwer Academic Publishers, P.O.Box 17, 3300 AA Dordrecht, The Nederlands, 1988.

Lichtenthaler, H. K.: Vegetation stress: an introduction to the stress concept in plants, J. Plant Physiol., 148, 4-14, 1996.

Lichtenthaler, H. K., and Schweiger, J.: Cell wall bound ferulic acid, the major substance of the blue-green fluorescence emission of plants, J. Plant Phys., 152, 272–282, doi:10.1016/S0176-1617(98)80142-9, 1998.

Mazzoni, M., Falorni, P., and Verhoef, W.: High-resolution methods for fluorescence retrieval from space, Opt. Express, 15, 15649–15663, 2010.

Mazzoni, M., Meroni, M., Fortunato, C., Colombo, R., and Verhoef, W.: Retrieval of maize canopy fluorescence and reflectance by spectral fitting in the O_2–A absorption band, Remote Sens. Environ., 124, 72–82, 2012.

McKibben, S. M., Strutton, P. G., Foley, D. G., Peterson, T. D., and White, A. E.: Satellite-based detection and monitoring of phytoplankton blooms along the Oregon coast, J. Geophys. Res., 117, 2012.

Meroni, M., Rossini, M., Guanter, L., Alonso, L., Rascher, U., Colombo, R., and Moreno, J.: Remote sensing of solar-induced chlorophyll fluorescence: review of methods and applications, Remote Sens. Environ., 113, 2037–2051, 2009.

Middleton, E. M., Cheng, Y.-B., Campbell, P. E., Huemmrich, K. F., Corp, L. A., Bernardes, S., Zhang, Q., Landis, D. R., Kustas, W. P., Daughtry, C. S. T., Alfieri, J. G., and Russ, A. L.: Multi-angle hyperspectral observations using fluorescence and PRI to detect plant stress and productivity in a cornfield, EARSeL eProceedings, Special Issue 2, 2015: 9th EARSeL Imaging Spectroscopy Workshop, 2015, Luxembourg City, Luxembourg, 13 pp., 2015.

Morrison, J. R., and Goodwin, D. S.: Phytoplankton photocompensation from space-based fluorescence measurements, Geophys. Res. Lett., 37, L06603, 2010.

Munro, R., Eisinger, M., Anderson, C., Callies, J., Corpaccioli, E., Lang, R., Lefebvre, A., Livschitz, Y., and Perez Albinana, A.: GOME-2 on MetOp: from In-Orbit Verification to Routine Operations, in: Proceedings of EUMETSAT Meteorological Satellite Conference, Helsinki, Finland, 12–16 June 2006.

O'Dell, C. W., Connor, B., Bösch, H., O'Brien, D., Frankenberg, C., Castano, R., Christi, M., Eldering, D., Fisher, B., Gunson, M., McDuffie, J., Miller, C. E., Natraj, V., Oyafuso, F., Polonsky, I., Smyth, M., Taylor, T., Toon, G. C., Wennberg, P. O., and Wunch, D.: The ACOS CO_2 retrieval algorithm – Part 1: Description and validation against synthetic observations, Atmos. Meas. Tech., 5, 99–121, doi: 10.5194/amt-5-99-2012, 2012.

O'Malley, R. T., Behrenfeld, M. J., Westberry, T. K., Milligan, A. J., Shang, S., Yan, J.: Geostationary satellite observations of dynamic phytoplankton photophysiology, Geophysi. Res. Lett., 41, 5052–5059, doi: 10.10002/2014GL060246, 2014.

Parazoo, N. C., Bowman, K., Frankenberg, C., Lee, J. E., Fisher, J. B., Worden, J., and Jones, D.: Interpreting seasonal changes in the carbon balance of southern Amazonia using measurements of XCO2 and chlorophyll fluorescence from GOSAT, Geophys. Res. Lett., 40, 2829-2833, 2013.

Parazoo N. C., Bowman K., Fisher J. B., Frankenberg C., Jones D. B., Cescatti A., Perez-Priego O., Wohlfahrt, G., and Montagnani, L.: Terrestrial gross primary production inferred from satellite fluorescence and vegetation models, Global Change Biol., 20, 3103–3121, doi:10.1111/gcb.12652, 2014.

Porcar-Castell, A., Tyystjärvi, E., Atherton, J., van der Tol, C., Flexas, J., Pfündel, E. E., Moreno, J., Frankenberg, C., and Berry, J. A.: Linking chlorophyll a fluorescence to photosynthesis remote sensing application: mechanisms and challenges, J. Exp. Botany, 65, 4065-4095, doi:10.1093/jxb/eru191, 2014.

Preusker, R., and Lindstrot, R.: Remote sensing of cloud-top pressure using moderately resolved measurements within the oxygen A band – a sensitivity study, J. Appl. Meteorol. Clim., 48, 1562–1574, 2009.

Rinderle, U., and Lichtenthaler, H.: The chlorophyll fluorescence ratio F690/F735 as a possible stress indicator, In: H. Lichtenthaler (Ed.), Applications of Chlorophyll Fluorescene in Photosynthesis Re- search, Stress Physiology, Hydrobiology and Remote Sensing, 189-196, Springer Netherlands, 1988.

Rothman, L. S., Gordon, I. E., Barbe, A., Benner, D. C., Bernath, P. F., Birk, M., Boudon, V., Brown, L. R., Campargue, A., Champion, J., Chance, K., Coudert, L. H., Dana, V., Devi, V. M., Fally, S., Flaud, J. M., Gamache, R. R., Goldman, A., Jacquemart, D., Kleiner, I., Lacome, N., Lafferty, W. J., Mandin, J., Massie, S. T., Mikhailenko, S. N., Miller, C. E., Moazzen-Ahmadi, N., Naumenko, O. V., Nikitin, A. V., Orphal, J., Perevalov, V. I., Perrin, A., Predoi-Cross, A., Rinsland, C. P., Rotger, M., Simecková, M., Smith, M. A. H., Sung, K., Tashkun, S. A., Tennyson, J., Toth, R. A., Vandaele, A. C., and Vander Auwera, J.: The HITRAN 2008 molecular spectroscopic database, J. Quant. Spectrosc. Rad. Trans., 110, 533–572, 2009.

Sanders, A. F. J. and de Haan, J. F.: Retrieval of aerosol parameters from the oxygen A band in the presence of chlorophyll fluorescence, Atmos. Meas. Tech., 6, 2725–2740, doi:10.5194/amt-6-2725-2013, 2013.

Sanders, A. F. J., de Haan, J. F., Sneep, M., Apituley, A., Stammes, P., Vieitez, M. O., Tilstra, L. G., Tuinder, O. N. E., Koning, C. E., and Veefkind, J. P.: Evaluation of the operational Aerosol Layer Height retrieval algorithm for Sentinel-5 Precursor: application to O_2 A band observations from GOME-2A, Atmos. Meas. Tech., 8, 4947–4977, doi:10.5194/amt-8-4947-2015, 2015.

Subhash, N. and Mohanan, C. N.: Curve-fit analysis of chlorophyll fluorescence spectra: application to nutrient stress detection in sunflower, Remote Sens. Environ., 60, 347–356, 1997.

Sun, Y., Fu, R., Dickenson, R., Joiner, J., Frankenberg, C., Gu, L., Xia, Y., and Fernando, N.: Satellite solar-induced chlorophyll fluorescence reveals drought onset mechanisms: Insights from two contrasting extreme events, J. Geophys. Res., 120, 2427–2440, doi:10.1002/2015JG003150, 2015.

Tilstra, L. G., Tuinder, O. N. E., and Stammes, P.: A new method for in-flight degradation corrections of GOME-2 Earth reflectance measurements, with application to the absorbing aerosol index, Proc. 2012 EUMETSAT Meteorol. Sat. Conf., http://www.temis.nl/airpollution/absaai, 2012.

Vasilkov, A., Joiner, J., and Spurr, R.: Note on rotational-Raman scattering in the O_2 A- and B-bands, Atmos. Meas. Tech., 6, 981–990, doi: 10.5194/amt-6-981-2013, 2013.

Verrelst, J., Rivera, J. P., van Der Tol, C., Magnani , F., Mohammed, G., Moreno, J.: Global sensitivity analysis of SCOPE v1.53 model: what drives canopy-leaving sun-induced fluorescence? Rem. Sens. Environ., 166, 8-21, 2015.

Westberry, T. K., Behrenfeld, M. J., Milligan, A. J., and Doney, S. C.: Retrospective satellite ocean color analysis of purposeful and natural ocean iron fertilization, Deep Sea Research Part I: Oceanographic Res. Pap., 73, 1–16, doi:10.1016/j.dsr.2012.11.010, 2013.

Wolanin, A., Rozanov, V. V., Dinter, T., No"el, S., Vountas, M., Burrows, J. P., and Bracher, A.: Global retrieval of marine and terrestrial chlorophyll fluorescence at its red peak using hyperspectral top of atmosphere radiance measurements: Feasibility study and first results, Remote Sens. Environ., 166, 243–261, doi:10.1016/j.rse.2015.05.018, 2015.

Yang, X., Tang, J., Mustard, J. F., Lee, J.-E., Rossini, M., Joiner, J., Munger, W., Kornfield, A., and Richardson, A. D.: Solar-induced chlorophyll fluorescence correlates with canopy photosynthesis on diurnal and seasonal scales in a temperature deciduous forest, Geophys. Res. Lett., 42, 2977-2987, doi: 10.1002/2015GL063201RR, 2015.

Yoshida, Y., Joiner, J., Tucker, C., Berry, J., Lee, J.-E., Walker, G., Reichle, R., Koster, R., Lyapustin, A., and Wang, Y.: The 2010 Russian drought impact on satellite measurements of solar-induced chlorophyll fluorescence: Insights from modeling and comparisons with parameters derived from satellite reflectances, Remote Sens. Environ., 166, 163–177, doi: 10.1016/j.rse.2015.06.008, 2015.

Zarko-Tejada, P. J., Miller, J. R., Mohammed, G. H., and Noland, T. L.: Chlorophyll fluorescence effects on vegetation apparent reflectance: I. Leaf-level measurements and model simulations, Remote Sens. Environ., 74, 582–595, 2000.

Zarco-Tejada, P. J., Pushnik, J. C., Dobrowski, S., Ustin, S. L.: Steady-state chlorophyll a fluorescence detection from canopy derivative reflectance and double-peak red-edge effects, Remote Sens. Environ., 84, 283-294, 2003.

Zhang, Y., Guanter, L., Berry, J. A., Joiner, J., van der Tol, C., Huete, A., Gitelson, A., Voigt, M., Koehler, P.: Estimation of vegetation photosynthetic capacity from space-based measurements of chlorophyll fluorescence for terrestrial biosphere models, Global Change Biol., 20, 3727–3742, doi:10.1111/gcb.12664, 2014.

Atmos. Meas. Tech. Discuss., doi:10.5194/amt-2015-387, 2016
Manuscript under review for journal Atmos. Meas. Tech.
Published: 18 January 2016

Atmospheric Measurement Techniques Discussions

Table 1. Statistical comparison of retrieved versus true values of SIF obtained with the simulated testing data set for different experiments (Exp); all fluorescence radiance units (indicated by *) are $\mathrm{mW\,m^{-2}\,nm^{-1}\,sr^{-1}}$. Retrievals are performed for an instrument with a given full-width at half-maximum (FWHM) line shape function, signal-to-noise ratio (SNR), number of principal components (#PCs), and fitting window from starting wavelength λ_1 to ending wavelength λ_2. Statistics given are the root-mean-squared difference (RMS diff.), correlation coefficient (r), mean difference (bias) of retrieved minus truth, standard deviation (σ), and slope (B) and intercept (A) of a linear fit (retrieved fluorescence = A + B · truth) (last two columns, respectively). Under the signal-to-noise ratio (SNR) heading, "nom." refers to the nominal model described in the text.

Exp	FWHM (nm)	SNR	#PCs	λ_1 (nm)	λ_2 (nm)	γ-band incl.	RMS diff. *	r	bias *	σ *	slope	intercept *
1	0.5	nom.	5	682	698	Y	0.97	0.90	-0.65	0.72	0.69	0.15
2	0.5	nom.	10	682	698	Y	0.62	0.96	-0.38	0.48	0.83	0.04
3	0.5	nom.	15	682	698	Y	0.55	0.95	-0.26	0.48	0.85	0.12
4	0.5	nom.	10	682	689	Y	0.60	0.93	-0.12	0.58	0.91	0.11
5	0.5	nom.	10	682	689	N	0.75	0.90	-0.27	0.70	0.88	0.03
6	0.5	no noise	10	682	698	Y	0.49	0.99	-0.38	0.31	0.83	0.04
7	0.5	no noise	10	682	689	Y	0.26	0.99	-0.12	0.24	0.91	0.10
8	0.5	no noise	10	682	689	Y[a]	1.13	0.69	0.46	1.03	0.73	0.88
9	0.5	no noise	10	682	689	N	0.22	1.00	-0.16	0.15	0.93	-0.01
10	0.5	2X nom.	10	682	698	Y	0.89	0.87	-0.39	0.80	0.83	0.04
11	0.3	nom.	10	682	698	Y	0.57	0.98	-0.41	0.39	0.81	0.09
12	0.3	nom.	10	682	689	Y	0.41	0.98	-0.23	0.34	0.89	0.05
13	0.1	nom.	5	682	686.7	N	0.29	1.00	-0.19	0.22	0.94	0.00
14	0.2	nom.	5	682	686.7	N	0.38	0.99	-0.18	0.33	0.95	-0.01
15	0.3	nom.	5	682	686.7	N	0.53	0.97	-0.18	0.50	0.95	-0.01
16	0.5	nom.	5	682	686.7	N	1.10	0.87	-0.23	1.07	0.94	-0.03
17	0.3[b]	nom.	5	682	686.7	N	0.67	0.95	-0.18	0.65	0.95	-0.01
18	0.3	nom.[c]	5	682	686.7	N	0.58	0.96	-0.01	0.57	0.96	0.06
19	0.5	nom.[c]	5	682	686.7	N	1.16	0.85	-0.17	1.15	0.91	0.12

[a] Used a flat solar spectrum

[b] Sampling of 0.2 nm instead of 0.1 nm

[c] Wavelength jitter of 0.01 nm simulated

Atmos. Meas. Tech. Discuss., doi:10.5194/amt-2015-387, 2016
Manuscript under review for journal Atmos. Meas. Tech.
Published: 18 January 2016

Atmospheric Measurement Techniques Discussions
Open Access

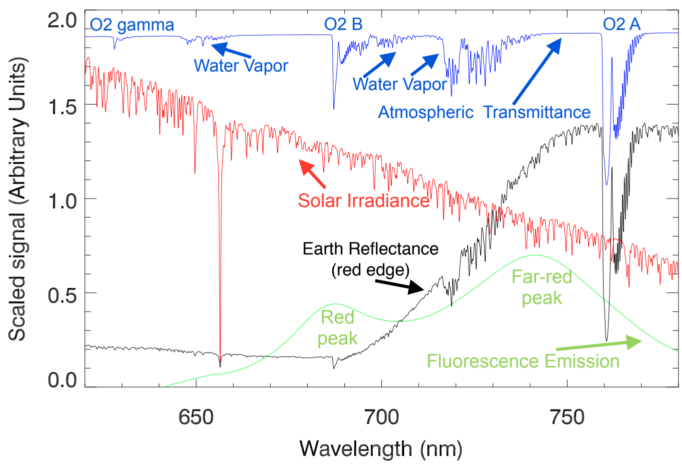

Figure 1. Simulated typical terrestrial spectra (atmospheric transmittance, reflectance, SIF emissions, and solar irradiance as a function of wavelength) computed for an instrument with FWHM = 0.3 nm.

Atmos. Meas. Tech. Discuss., doi:10.5194/amt-2015-387, 2016
Manuscript under review for journal Atmos. Meas. Tech.
Published: 18 January 2016

Atmospheric Measurement Techniques
Discussions

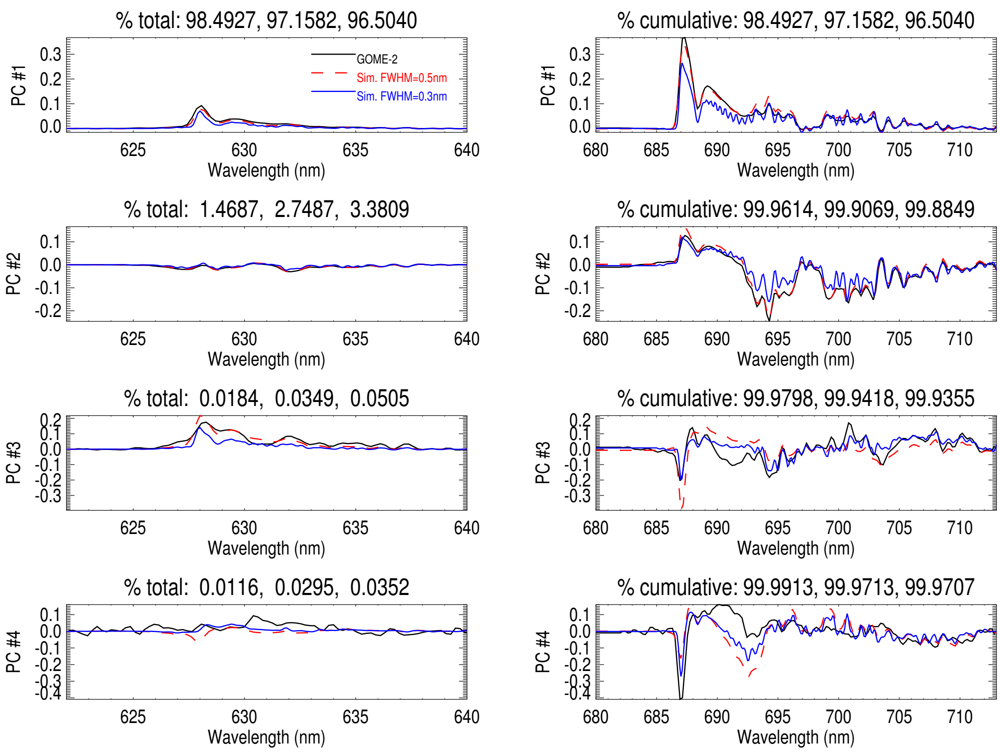

Figure 2. Leading principal components (PCs) of simulated (Sim.) and actual GOME-2 reflectance spectra (from 1 July 2012, black) for spectral windows encompassing the oxygen γ band (left panels) and B-band (right panels). Simulated data are for a GOME-like instrument (red lines) with FWHM = 0.5 nm (red) and a higher spectral resolution instrument with FWHM = 0.3 nm (blue); numbers in the top titles are the variance explained in terms of percent of the total and cumulative percent of the total with numbers for GOME-2, simulated FWHM = 0.5 nm, and FWHM = 0.3 nm, respectively.

Atmos. Meas. Tech. Discuss., doi:10.5194/amt-2015-387, 2016
Manuscript under review for journal Atmos. Meas. Tech.
Published: 18 January 2016

Atmospheric Measurement Techniques
Discussions
Open Access
EGU

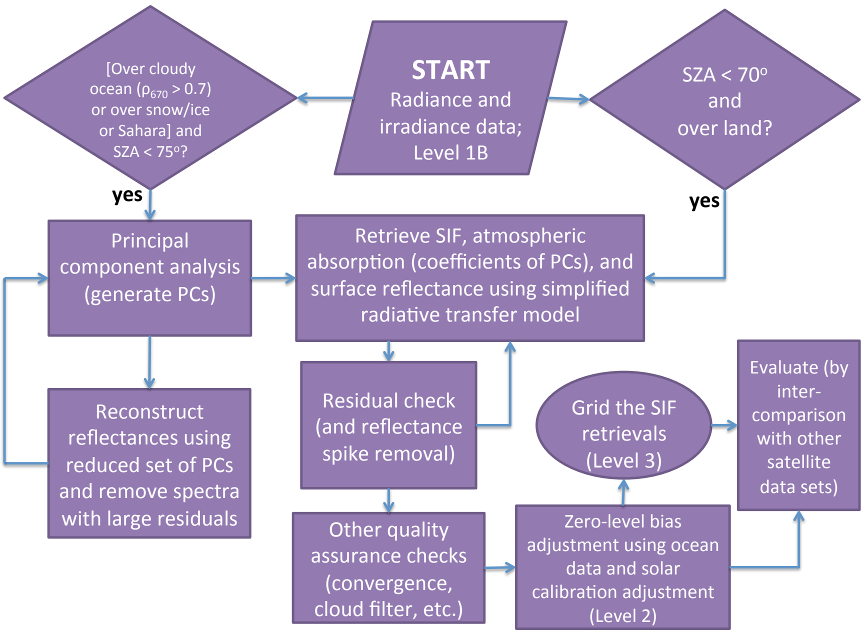

Figure 3. Flow diagram of the basic steps used to produce SIF data sets.

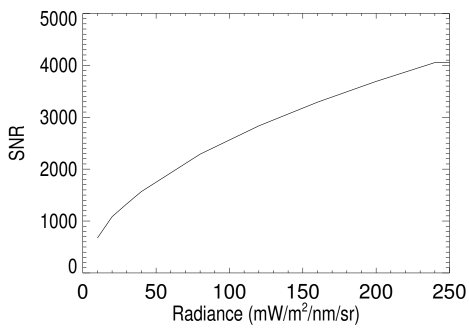

Figure 4. Nominal signal-to-noise ratio (SNR) used in simulations.

Atmos. Meas. Tech. Discuss., doi:10.5194/amt-2015-387, 2016
Manuscript under review for journal Atmos. Meas. Tech.
Published: 18 January 2016

Atmospheric Measurement Techniques
Discussions

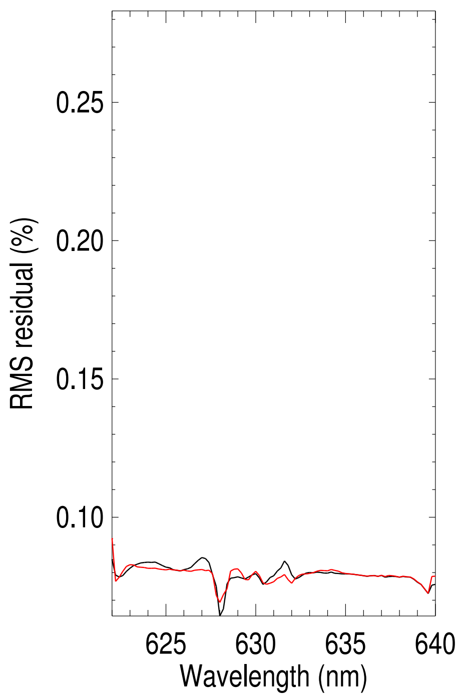

Figure 5. Root mean squared (RMS) of simulated radiance residuals (observed minus computed, in % of radiance) at wavelengths in and around the O_2 γ-band (left) and B-band (right) from the testing dataset with FWHM = 0.5 nm and nominal noise model when fluorescence (SIF) is fit/retrieved (red) and when it is not (black).

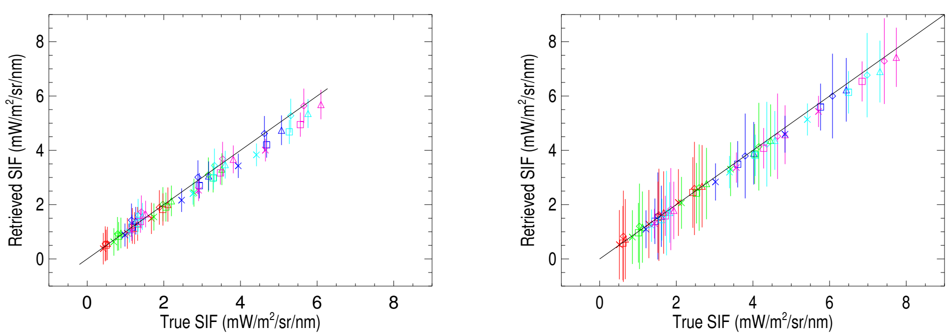

Figure 6. Fluorescence retrievals from simulated data (y-axis) using wavelengths between 682 and 689 nm along with wavelengths surrounding the O_2 γ-band (left) and using wavelengths between 682 and 686.5 nm (right) for an instrument with FWHM = 0.5 nm and with the nominal noise model. Fluorescence is averaged over the fitting window used in the retrieval (different for left and right panels) and compared with the “truth" (x-axis) averaged in the same way. Standard deviations are shown with vertical bars. Different symbols are shown for the various values of chlorophyll content and different colors are for the various values of leaf area index.

Atmos. Meas. Tech. Discuss., doi:10.5194/amt-2015-387, 2016
Manuscript under review for journal Atmos. Meas. Tech.
Published: 18 January 2016

Atmospheric Measurement Techniques Discussions
Open Access

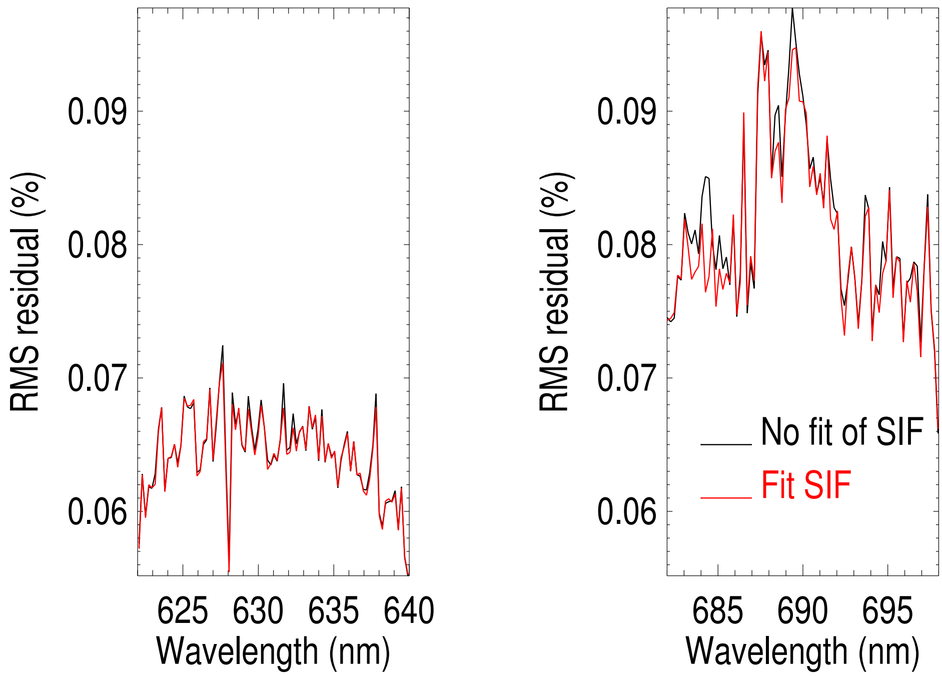

Figure 7. Similar to Fig. 5 for actual GOME-2 radiance residuals (RMS) for pixels with moderate to high amounts of vegetation (NDVI > 0.5) for a single day (01 July 2007).

Atmospheric Measurement Techniques
Discussions
Open Access

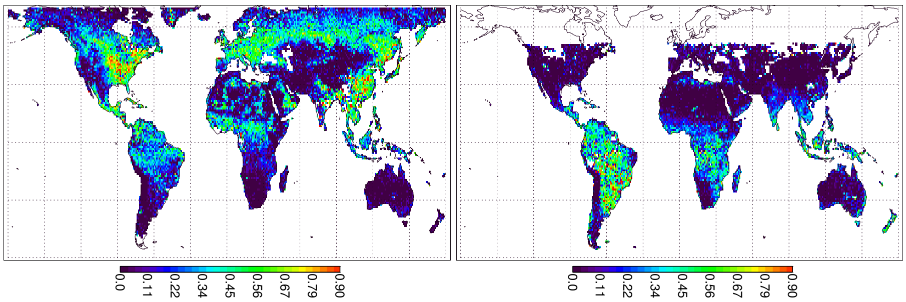

(a) SCIAMACHY solar line red SIF retrievals using fitting window 682-686.5 nm for July (left) and December (right) 2009.

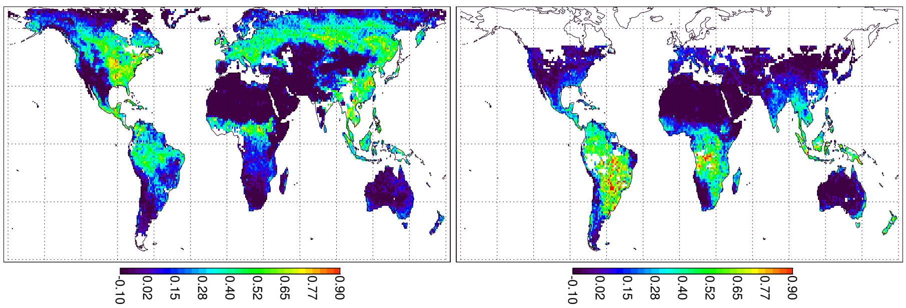

(b) Similar to (a) but using fitting windows in O_2 γ (622–640 nm)- and B-bands (682–692 nm).

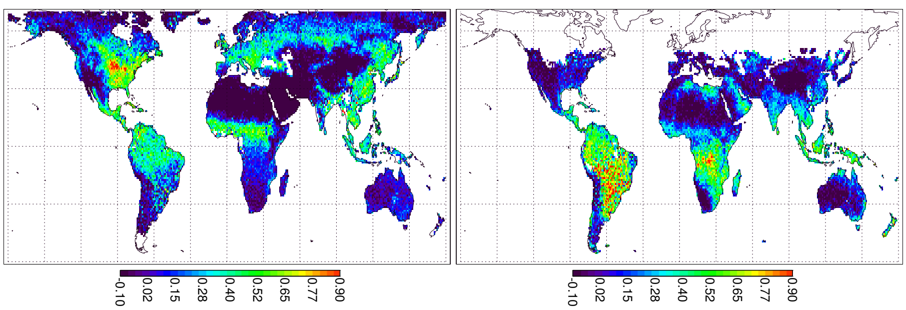

(c) Similar to (b) but using GOME-2.

Figure 8. Global composites of red SIF from SCIAMACHY and GOME-2 binned in 1° cell boxes with zero-level adjustment.

Atmos. Meas. Tech. Discuss., doi:10.5194/amt-2015-387, 2016
Manuscript under review for journal Atmos. Meas. Tech.
Published: 18 January 2016

Atmospheric Measurement Techniques
Open Access
Discussions

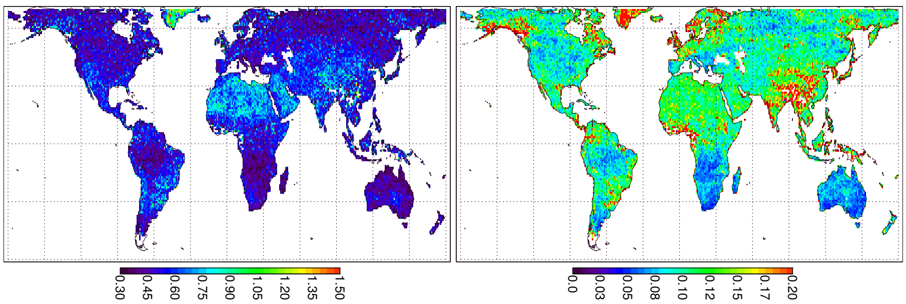

(a) Grid cell standard deviation (left) and standard error (right) for SCIAMACHY solar line red SIF retrievals (682–686.5 nm).

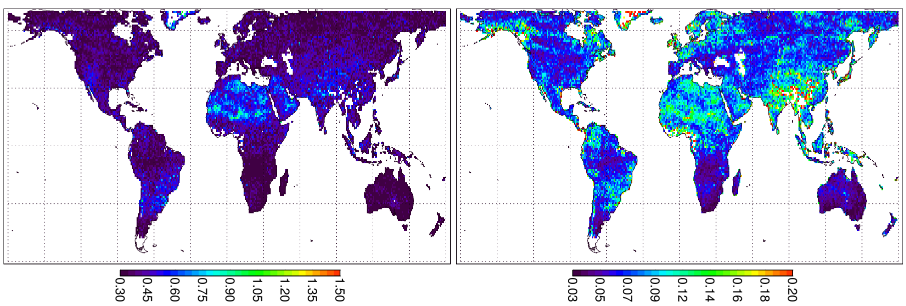

(b) Similar to (a) but for SCIAMACHY O_2 band red SIF retrievals (622–640 nm and 682–692 nm).

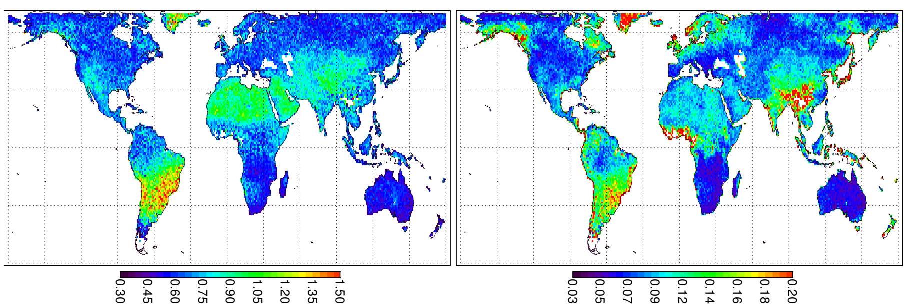

(c) Similar to (b) but for GOME-2.

Figure 9. Global maps of red SIF retrieval statistical parameters in 1° grid cells for July 2007.

Atmos. Meas. Tech. Discuss., doi:10.5194/amt-2015-387, 2016
Manuscript under review for journal Atmos. Meas. Tech.
Published: 18 January 2016

Atmospheric Measurement Techniques
Open Access
Discussions

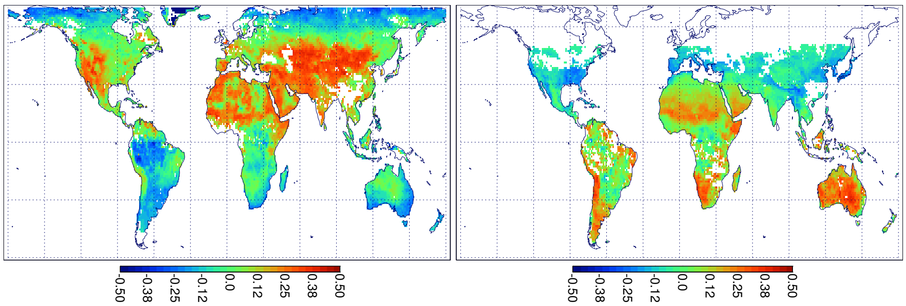

(a) Zero-level adjustment for July (left) and December (right) 2007 for SCIAMACHY solar line red SIF retrievals (682–686.5 nm).

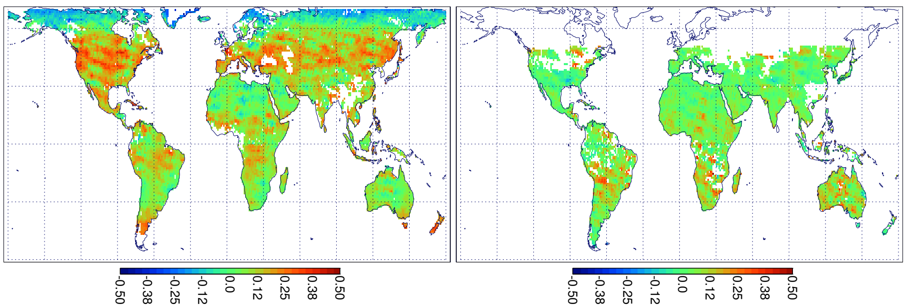

(b) Similar to (a) but for SCIAMACHY O_2 band red SIF retrievals (622–640 nm and 682–692 nm).

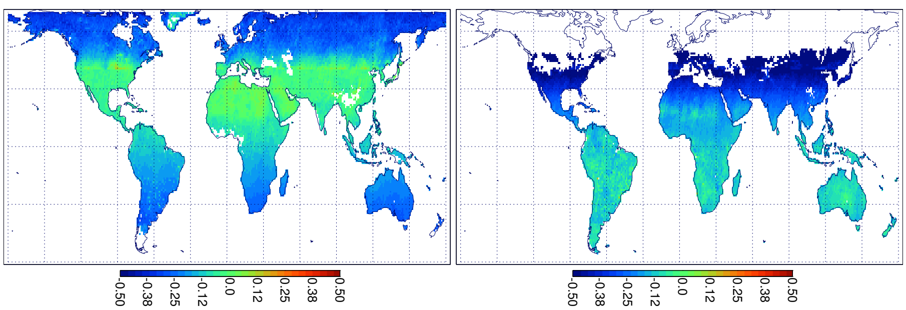

(c) Similar to (b) but for GOME-2.

Figure 10. Global maps of the zero-level adjustment July (left) and December (right) 2007.

Atmos. Meas. Tech. Discuss., doi:10.5194/amt-2015-387, 2016
Manuscript under review for journal Atmos. Meas. Tech.
Published: 18 January 2016

Atmospheric Measurement Techniques Discussions

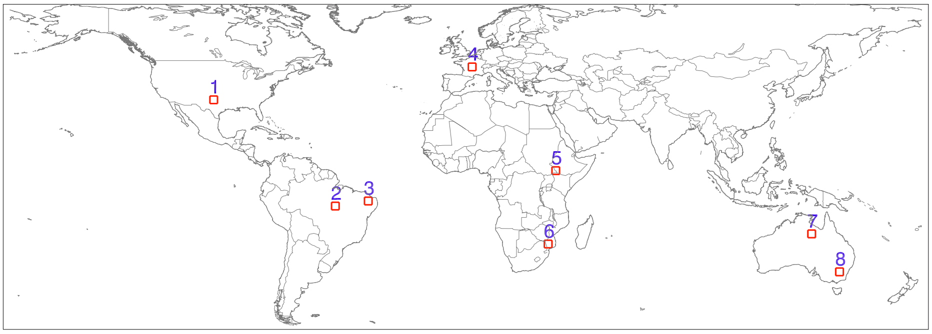

Figure 11. Map showing boxes where SIF time series will be examined.

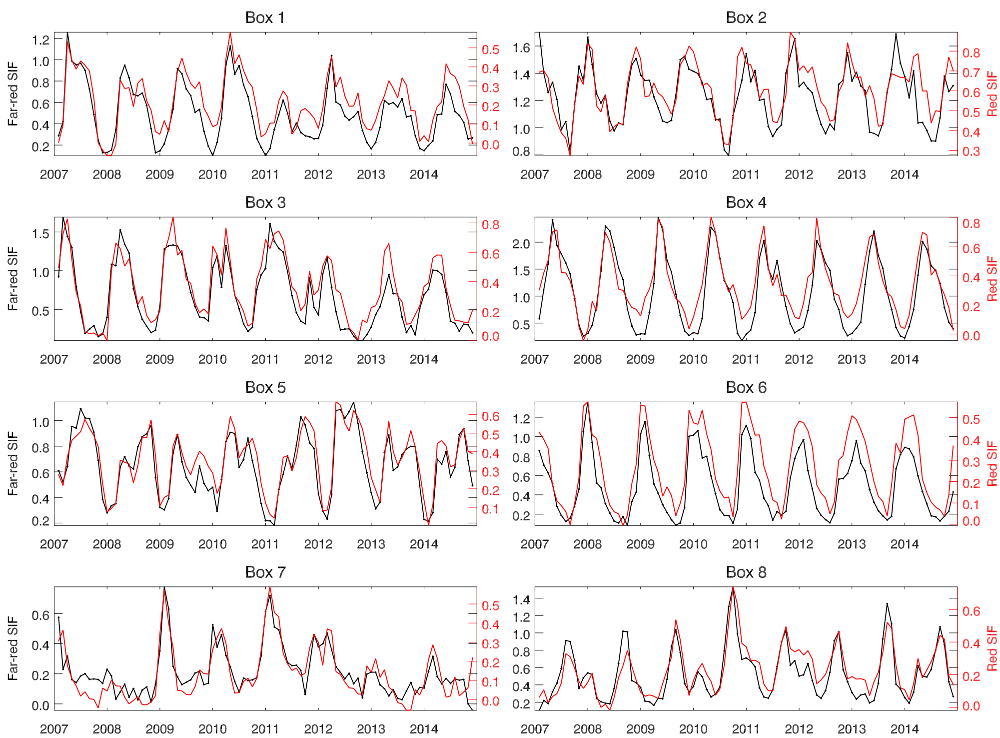

Figure 12. Time series of monthly red (red, right axes) and far-red SIF (black, left axes) in mW/m^2/nm/sr from GOME-2 for 8 boxes shown in Fig. 11. Axes are specified to align the maximum values.

Atmos. Meas. Tech. Discuss., doi:10.5194/amt-2015-387, 2016
Manuscript under review for journal Atmos. Meas. Tech.
Published: 18 January 2016

Atmospheric Measurement Techniques
Discussions

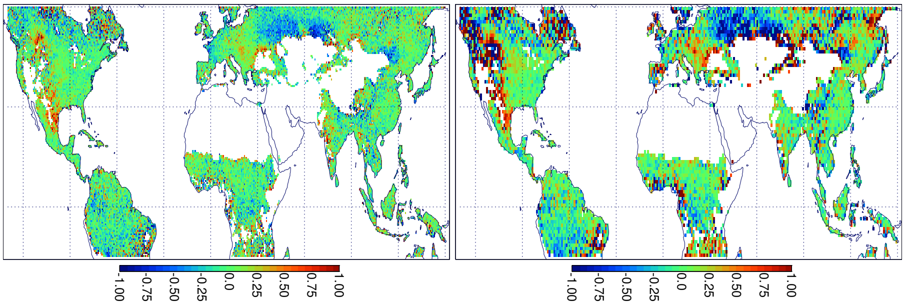

(a) SIF anomalies (in terms of fractional amount of climatological values) for August 2010 for far-red (left) and red (right) GOME2 SIF retrievals.

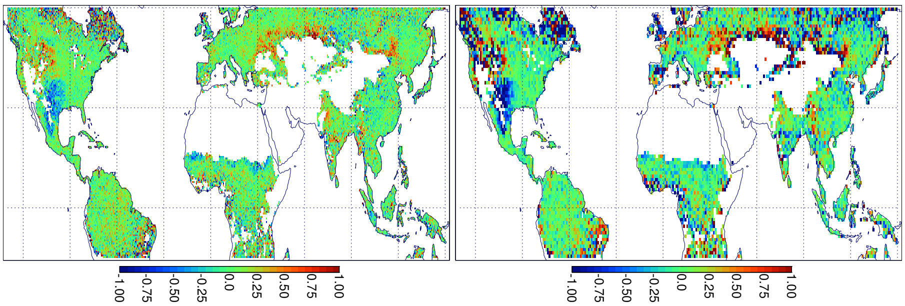

(b) Similar to (a) but for August 2011.

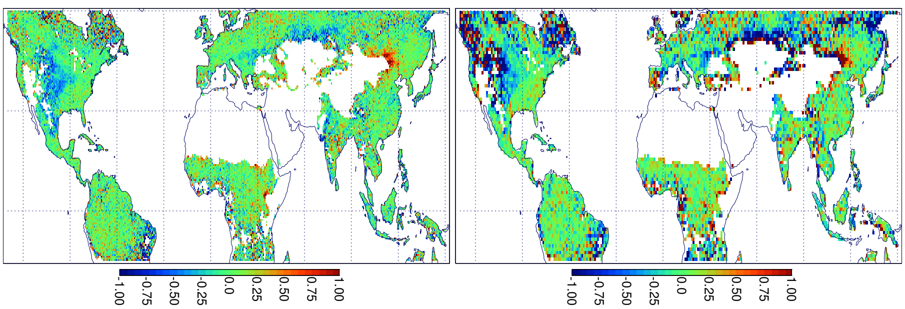

(c) Similar to (b) but for August 2012.

Figure 13. Global SIF anomaly maps (in terms of fractional amount of climatological values) for August 2010, 2011, and 2012 (top to bottom) for GOME-2 far-red (left) and red (right) retrievals.

Atmospheric Measurement Techniques
Discussions

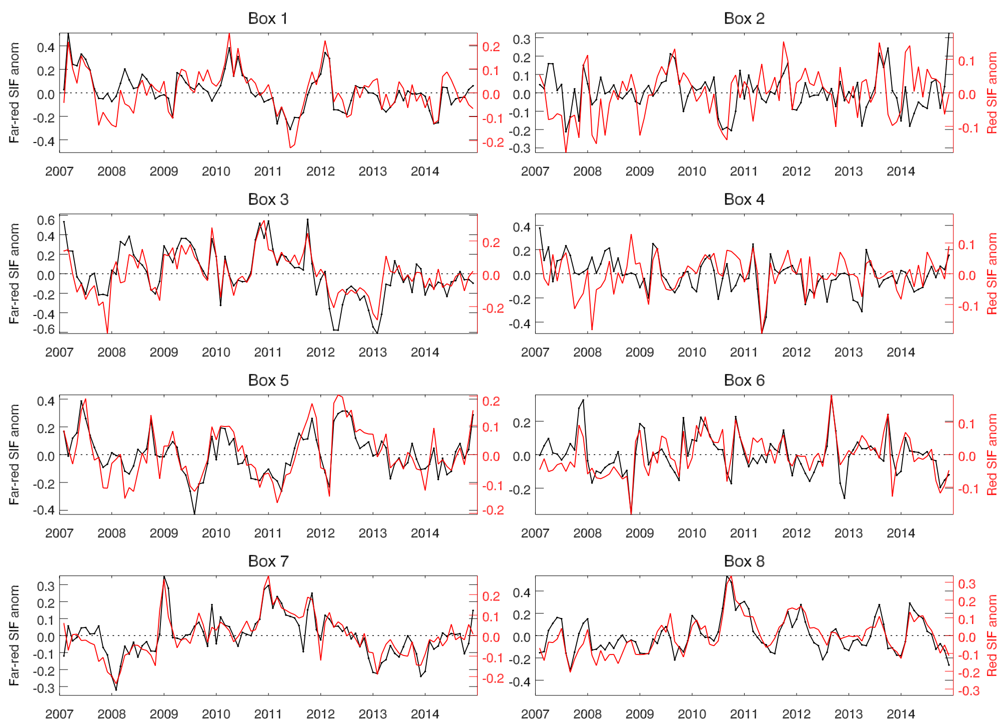

Figure 14. Similar to Fig. 12 but showing time series of red and far-red SIF monthly anomalies (in mW/m^2/nm/sr) from GOME-2 for 8 boxes shown in Fig. 11.

Atmos. Meas. Tech. Discuss., doi:10.5194/amt-2015-387, 2016
Manuscript under review for journal Atmos. Meas. Tech.
Published: 18 January 2016

Atmospheric Measurement Techniques
Open Access
Discussions

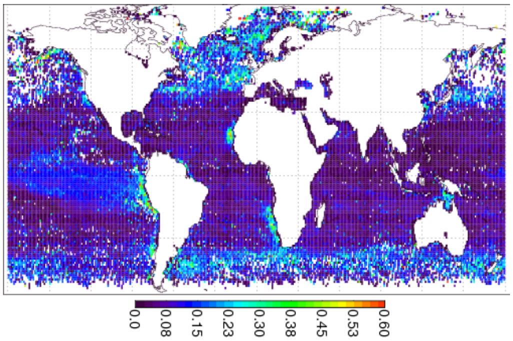

(a) SCIAMACHY simplified nFLH.

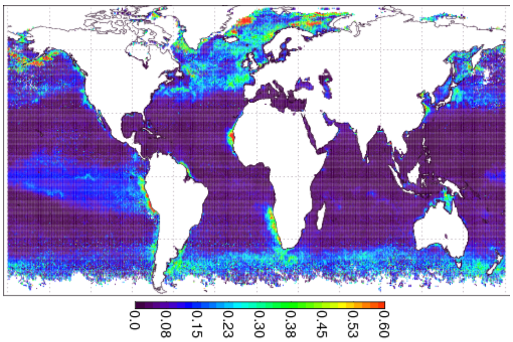

(b) Similar to (a) but for GOME-2.

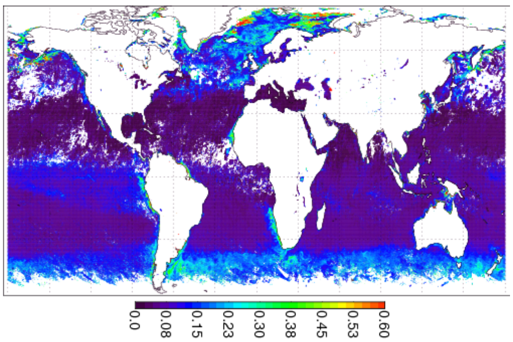

(c) MODIS nFLH.

Figure 15. Monthly mean (simplified) normalized fluorescence line height (nFLH) from SCIAMACHY (top), GOME-2 (middle), and Terra MODIS (bottom) in mW/m^2/sr/nm for May 2007. SCIAMACHY and GOME-2 are gridded to spatial resolutions of 0.5° and 1°, respectively. MODIS data were obtained at a 9 km spatial resolution. No zero-level adjustments are made to the retrievals.

Atmos. Meas. Tech. Discuss., doi:10.5194/amt-2015-387, 2016
Manuscript under review for journal Atmos. Meas. Tech.
Published: 18 January 2016

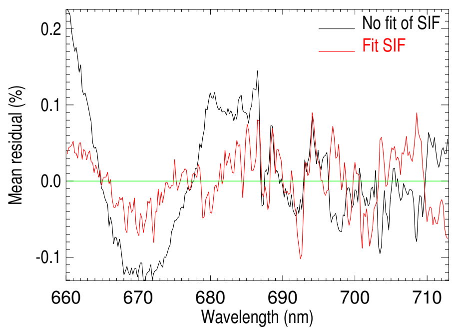

Figure 16. Similar to Fig. 7 but showing the mean of the residuals within the full band algorithm fitting window for ocean pixels with moderate to high amounts of ocean fluorescence (FLH > 0.4 mW/m^2/nm/sr) for a single day (01 July 2007).